ABSTRACT

Production of meson, baryon and light nuclei (A=2, 3): investigating freeze-out dynamics and roles of energetic quarks and gluons in Au+Au collisions at RHIC

Haidong Liu
University of Science and Technology of China
2007

In relativistic heavy-ion collisions, a high temperature matter with strong interactions is produced. The Lattice QCD calculations predict a phase transition from hadronic matter to a quark-gluon plasma state, where the quarks are believed to be deconfined. In this thesis, we report the recent STAR measurements on identified hadron and light nuclei production in Au+Au 200 GeV collisions at RHIC.

Light nuclei, which have small binding energies among the constituent nucleons, are believed to be formed at the moment of the thermal freeze-out. Therefore, the production of light nuclei provides a tool to measure the freeze-out properties. Benefitting from the high statistic data sample taken in RHIC Run IV, we have measured the $^3He(\overline{^3He})$ p_T spectra and v_2 at intermediate p_T region ($2 < p_T < 6\ GeV/c$) and $d(\bar{d})$ p_T spectra and v_2 at $1 < p_T < 4\ GeV/c$. The coalescence parameters B_2 and B_3 are extracted. The low p_T ($0.2 < p_T < 1\ GeV/c$) $\bar{d}$ v_2 has also been measured. We find that B_2 has the similar value with $\sqrt{B_3}$. It indicates the $d(\bar{d})$ and $^3He(\overline{^3He})$ have a similar freeze-out time. We compare the B_2 and $\sqrt{B_3}$ to the pion freeze-out volume measured by HBT study. It is found that the B_2 and $\sqrt{B_3}$ are inverse proportional to the pion freeze-out volume in various centrality collisions. The freeze-out volume is found to be constant with $\sqrt{s_{NN}}$ at $\sqrt{s_{NN}} > 20\ GeV$ when we compare our results to the low energy results. The $d + \bar{d}$ v_2 is found to follow the atomic mass number (A) scaling within errors and we observe a deviation of $^3He + \overline{^3He}$ v_2 from the A scaling. The first negative v_2 at RHIC has been observed for low p_T $\bar{d}$ in mid-central collisions. This is consistent with a large radial flow scenario.

We have systematically studied the anti-baryon phase space density inferred from $\bar{d}/\bar{p}$ measurements in various collision systems at various energies. It is found that the anti-baryon density at the final-state coalescence saturates when the process from different collisions involving gluons.

We use the particle identification capability of the STAR TPC and TOF detectors to measure the $\pi^{\pm}$ and $p(\bar{p})$ spectra in large transverse momentum range ($0.3 < p_T < 12\ GeV/c$). The relative baryon enhancement is observed in central collision and this can be explain by the partonic coalescence phenomena. At high p_T, the suppressions of meson and baryon are observed to be the same, which are not consistent with the partonic energy loss calculation of pQCD. This points to possible phenomena beyond pQCD energy loss in a strong interacting matter.

中文摘要

介子、重子和轻核（氘，氦－3）的产生：RHIC 能区金金对撞实验中对系统 freeze-out 动力学以及高动量部分子性质和作用的研究

刘海东

中国科学技术大学， 2007 年 4 月

量子色动力学（QCD）是一种描述强相互作用的基本的规范场理论。格点 QCD 计算预言在高温和低重子密度的条件下会产生从普通的强子物质到一种高温、高密度、夸克解禁闭、局部热化的新物质状态－夸克胶子等离子体（QGP）的相变。美国布鲁克海汶国家实验室（BNL）的相对论重离子对撞机（RHIC）上已往的结果显示，正如格点 QCD 所预言，RHIC 试验中的相对论重离子对撞产生了一种新的高温、高密度的物质，这种物质不能用强子物质的自由度来描述。在 STAR 探测器上，通过联合我们自己研制的飞行时间谱仪（样机）（MRPC－TOF）和时间投影室（TPC）中电离能损（dE/dx），π介子、质子、反质子和轻核能够在大横动量区间被鉴别出来。在本文中，我们将给出 RHIC 金金 200GeV 对撞试验中，关于π介子、质子、反质子和轻核产生的最新结果。

在对撞末态粒子中有少量轻核，由于这些轻核的结合能很低，所以它们只能在对撞的末期通过核子的相互结合产生。因此，轻核的产生为我们研究系统的末态性质和末态演化提供了有利的工具。我们通过对氘、氦－3 以及它们的反粒子在中横动量区间的不变产额和椭圆流的测量的深入研究，我们得到轻核的结合参数（B_2 和 B_3）。我们发现 B_2 与 $\sqrt{B_3}$ 具有相似的值，这表示了氘、氦－3 以及它们的反粒子有相似的 freeze-out 时刻。我们还把轻核的结合参数与π介子的 HBT 结果进行比较，发现在不同中心度对撞中，轻核的结合参数和π介子的 freeze-out 体积成反比。我们系统地比较了不同对撞能量下的 B_2 的值，我们发现当 $\sqrt{s_{NN}} > 20GeV$ 时，氘核的 freeze-out 体积不随对撞能量的变化而改变。通过对中横动量轻核椭圆流的测量，我们发现氘核与反氘核的 v_2 在误差范围内服从组分核子数（A）的标度不变性；而氦核与反氦核的 v_2 却在一定程度上偏离核子数的标度不变性。我们还测量了低横动量的反氘核的 v_2，这是 RHIC 上观测到的第一个负值椭圆流。通过对 Blast-wave 模型的比较和研究，我们发现重粒子（氘）的负值椭圆流与大径向流图像相吻合。另外，通过对不同对撞系统（AA, pA, pp, γp , e^+e^- ）和不同对撞能量中反氘核和反质子的产额比（$\bar{d}/\bar{p}$）的研究，我们发现在各种反应机制中，胶子的参与是（反）重子产生的重要条件。

在本文中，我们还将给出利用 MRPC－TOF 时间飞行谱仪探测器（样机）的π、p 数据和时间投影室中获得的带电粒子的电离能量损失(dE/dx)的数据，发展了一种可以鉴别高动量区间的π介子和质子的新技术，将 STAR 的π，p 的粒子鉴定横动量区间扩展到 12GeV/c。通过测量带电强子（$\pi^{\pm}, p, \overline{p}$）的横动量谱（$0.3 < p_T < 12GeV/c$）。我们观察到在中横动量区间有相关重子产额加强的现象，这可以用部分子的结合模型来解释。pQCD 的计算显示在穿过高温、高密的 QGP 时，高能胶子会比高能轻夸克（uds）损失更多的能量，因而 pQCD 预言在高横动量区间，中心对撞事例中重子产额会比介子有更大的压低。而我们的测量结果显示在高横动量区间，重子产额与介子产额有着相同大小的压低，这一现象揭示了夸克和胶子在 QGP 中的能损(dE/dx)可能与微扰 QCD 能损模型的预言不符，从而为高能部分子在 QGP 中的能损机制提供全新的实验现象。

Production of meson, baryon and light nuclei (A=2, 3): investigating freeze-out dynamics and roles of energetic quarks and gluons in Au+Au collisions at RHIC

A Dissertation
Presented to the Faculty of the Graduate School
of
University of Science and Technology of China
in Candidacy for the Degree of
Doctor of Philosophy

By
Haidong Liu

Dissertation Director: Prof. Xiaolian Wang
Off-campus Co-adviser: Dr. Zhangbu Xu

2007

Acknowledgments

First, I would like to thank my advisor, Prof. Xiaolian Wang for introducing me into this field, helping me at the very beginning and offering me the opportunity to participant the STAR data analysis and the related work. I appreciate her continuous support in the last six years. I would like to thank Dr. Zhangbu Xu, the co-advisor of my PhD research. His enormous physics knowledge and serious attitude on science give me a deep impression. He showed exemplary patience and understanding during my initial struggles with the STAR data analysis. I feel particularly lucky to have worked with him because he is not only an advisor in physics but also a friend and a mentor in life.

Special thanks to Dr. Nu Xu for his guidance and fruitful discussions in the last two years. I also thank Dr. Hans-Georg Ritter, Dr. Nu Xu and Dr. Tim Hallman for offering me the great opportunity to work and study in BNL.

My gratitude also goes Prof. Hongfang Chen, Prof. Zizong Xu and Prof. Ziping Zhang. I learnt a lot from them and I appreciate their kindness help and enlighten. Thank Prof. Jian Wu and Dr. Ming Shao for the fruitful discussions in my work. I would also like to thank Prof. Cheng Li for his help on the hardware.

Many thanks to Dr. Jing Liu and his wife Haiyin Jiang. They treat me like a family when I was in BNL. Dr. Jing Liu also taught me a lot on the software. I also thank Dr. Haibin Zhang and Dr. Aihong Tang. They offered me great help on both physics and my living when I was in BNL. I would like to thank Prof. Yi Wang and Dr. Jing Liu for teaching me driving, which is very useful in the last two years. Thanks!

I would like to thank my friends Dr. Xin Dong and Dr. Lijuan Ruan. They could always provide me the best and fast answers when I was trapped in the analysis. Grateful acknowledgements to my dear friends Dr. Chen Zhong, my classmate Dr. Yifei Zhang, Dr. Yan Lu, Jiaxu Zuo and Jiayun Chen for the joyful time we had together. Thanks a lot!

Many thanks to Dr. YanE Zhao and Yi Zhou. I appreciate their hospitable help on my living. I would like to thank my classmate Dr. Qing Shan, Zebo Tang, Yao Ming and the whole high energy group in USTC for their hardwork on the MRPC production and testing. Thank all other STAR collaborators for obtaining beautiful detector performance and data. Particularly thank STAR TOF group for their super efforts on making this new detector function well.

Finally, I express my deep gratitude to my parents for their sacrifice and support. Their endless love, support and encouragement have always been the most important part of my life.

Contents

List of Figures

Chapter 1

Introduction

1.1 QCD and the deconfined quark matter

Matter is made of leptons, quarks, and force mediators. Quarks, which are the building blocks of nucleons, carry a property analogous to electric charge called color. The theory that describes the forces between colored objects and that is thought to be the correct theory for strong interaction is called quantum chromodynamics (QCD). In QCD, just as the electromagnetic force is carried by photons, the strong force (or color force) is carried by gluons. However, whereas photons carry no electric charge, gluons do carry color charge so they can interact directly with each other. The electrodynamic coupling constant $\alpha = \frac{1}{137}$ but the strong coupling constant α_s varies with the momentum transfer of the strong interaction. Fig. 1.1 shows an α_s measurements [1] compared to the QCD prediction.

As a consequence of the direct gluon-gluon coupling the effective coupling constant for the strong force becomes smaller at shorter distances. This effect is known as asymptotic freedom. Asymptotic freedom means the force between quarks is stronger at larger distances so quarks seem to remain confined to a small ($\sim$1 fm^3) region in colorless groups of two (mesons) or three (baryons). Because the effective strong coupling is only small at short distances, perturbation theory can only be used with QCD for interactions involving large momentum transfers (i.e. hard processes). Although

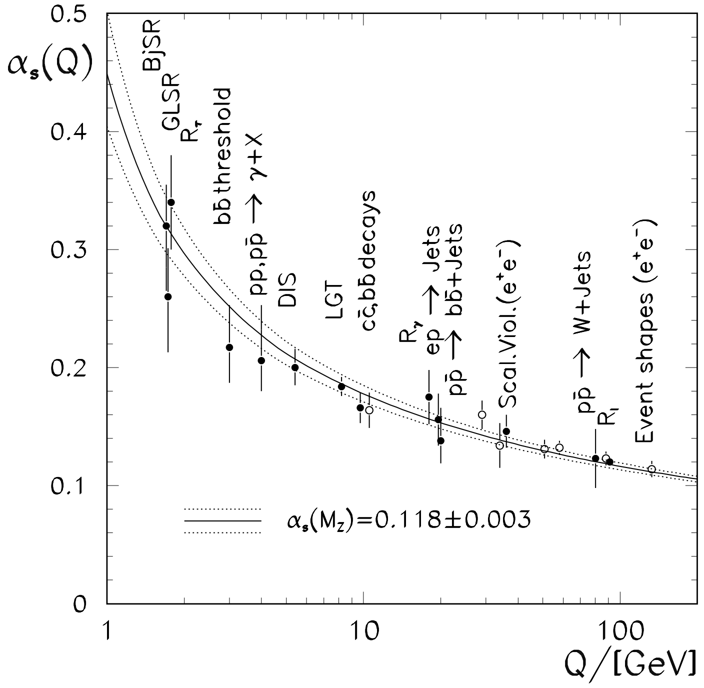

Figure 1.1: Running of the strong coupling constant established by various types of measurements at different scales, compared to the QCD prediction for $\alpha_s(M_z) = 0.118 \pm 0.003$.

perturbative QCD (pQCD) is in very good agreement with experimental observations involving hard processes (see Fig. 1.2 from PDG data book [52]), it fails to calculate QCD predictions for the processes that dominate the universe at present: soft processes.

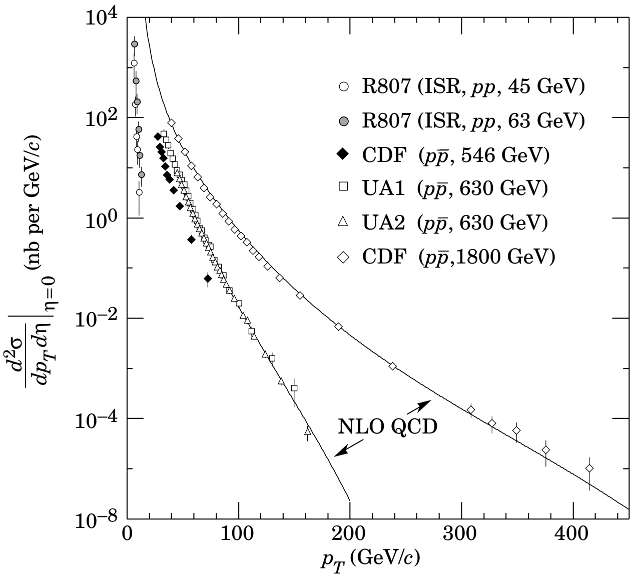

Figure 1.2: Differential cross-sections for single jet production at pseudo-rapidity $\eta = 0$ as a function of the jet transverse momentum p_T in proton (anti-)proton collisions. Jets are somewhat collimated sprays of particles produced when quarks or gluons collide, transfer (and carry away) a lot of momentum, and then fragment into a spray of hadrons. The curves represent pQCD calculations for the collisions at center-of-mass energy $\sqrt{s} = 630$ and 1800 GeV.

Explicit QCD Lagrangian calculations of the force between quarks can only be made in the limits of weak and strong coupling. To understand the behavior of colored objects where pQCD is not a valid approximation, physicists rely on numerical path integrals of the QCD Lagrangian on a discretized lattice in four-dimensional Euclidean space-time. It is the formulation of Lattice QCD with a strong coupling approximation that first demonstrated how quarks are confined [3].

In principle, the lattice formulation of QCD can be used to perform numerical calculations for all physical regimes. In practice, however, there are regimes where approximations used to simplify the calculations fail and the computations become technically very challenging.

In the strong coupling regime the energy required to separate two quarks increases fast with the distance between them. As a result, we have never observed deconfined quarks (i.e. free quarks, which can move in a volume much larger than the volume of a proton.) Recent advances in the formulation of thermodynamical lattice QCD at finite temperature and density however, suggests that when sufficiently high temperature and density are reached, quarks become effectively deconfined. Fig. 1.3 [4] shows that the ratio of the energy density scaled by T^4. Where ϵ is the energy density and T is the system temperature. ϵ/T^4 quickly increases at a critical temperature T_C. The magnitude of ϵ/T^4 reflects the number of degrees of freedom in the thermodynamic system. The rise corresponds to a transition in the system to a state where the quarks and gluons have become relevant degrees of freedom.

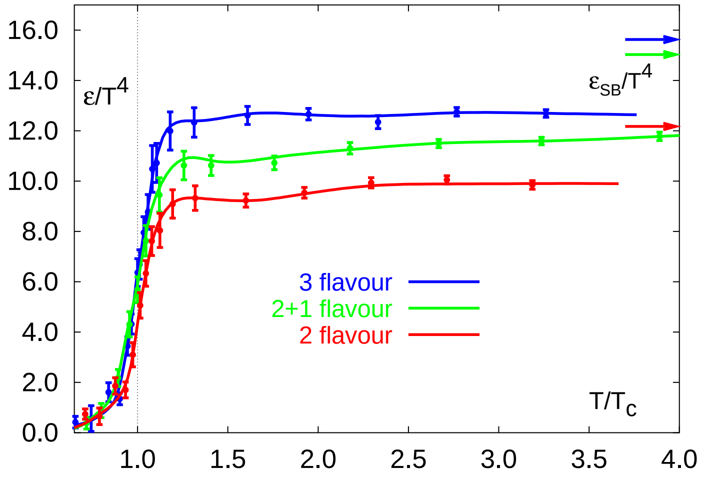

Figure 1.3: The energy density in QCD from lattice calculations. When the temperature T reaches the critical temperature T_c, the number of degrees of freedom rapidly rises indicating that quarks and gluons become relevant degrees of freedom. The arrows represent the Stefan-Boltzmann values for asymptotically high temperature.

1.2 Relativistic heavy-ion collisions

The creation and study of bulk matter made of deconfined quarks and gluons (quark-gluon plasma or QGP) was one of the prime motivations for building the Relativistic Heavy-Ion Collider (RHIC). The interaction of high-energy, colliding beams of heavy nuclei generates matter of extreme density and temperature. The temperatures and densities reached are expected to be similar to those thought to have prevailed in the very early universe, prior to the formation of protons and neutrons. The observation and study of matter in these conditions will be relevant to the nuclear physics community, the astrophysics community and the high-energy physics community. One also expects this research to have a significant impact on many in the general public since the nature of our universe at the earliest stages and the transitions that produced the matter we are familiar with today are interesting to most naturally curious or inquisitive people.

Early results from RHIC experiments reveal new nuclear phenomena at temperatures and densities well into the range where quarks and gluons (rather than baryons and mesons) are expected to define the relevant degrees of freedom. The first measurements of head-on collisions ar RHIC energies, with nuclei as heavy as gold, have already taken us a major step towards the seeking of quark gluon plasma. It has been found that different regions reveal dramatically different dynamics at RHIC. In the soft sector (about $p_T \leq 2\ GeV/c$), soft processes dominate and the multiplicities, yield, momentum spectra and correlations of hadrons reflect the properties of the bulk, for example its initial conditions, its degree of thermalization and its equation of state. In the sector of hard processes (about $p_T \geq 5\ GeV/c$), the interaction of energetic particles produced in initial hard scattering processes with the medium provides a unique, penetrating probes for the matter produced at RHIC. In the intermediate p_T region, where soft processes interplay with hard processes, the study of hadron production explores the hadronization processes in heavy-ion collisions and provide important information of the system evolution. A comprehensive summaries of the RHIC physics results can be found in the STAR white paper [5].

1.3 Light nuclei production

Relativistic heavy ion collisions create high energy density and high baryon density in the reaction zone. Light nuclei and their antiparticles can be produced by the recombination of created nucleons and anti-nucleons or stopped nucleons [6, 7, 8, 9]. This recombination process is called final-state coalescence. Since the binding energy of nucleus is quite small (e.g. 2.2 MeV for d and 7.7 MeV for ^3He), light nuclei cannot survive when the interactions between nucleons and other particles are strong. Therefore, the light nuclei formation can only happen at the late stage of the evolution when the interactions are weak. Hence, the production of nucleus provides a tool to measure baryon distribution at the thermal freeze-out where the interactions between particles are weakening. Since the probability of coalescence of a particular nuclear system (d, ^3He, etc.) depends on the properties of the hadronic system formed at late stage as a result of the collision, its evolution and hadronization, the study of the coalescence process is useful in elucidating those properties. For example, in a coalescence model, the coalescence probability depends on the temperature, baryon chemical potential (essentially the baryon density), and the size of the system, as well as the statistical weight (degeneracy) of the coalesced nucleus [10]. From the measurement of the nucleus production, we will be able to construct the thermal freeze-out in the (T, μ_B) phase diagram [7]. Together with the measurements of other particle yields from which the statistical model can construct the chemical freeze-out, we will be able to have a better understanding of how the system evolves from chemical to thermal freeze-out.

In the coalescence picture the cluster momentum distribution is related to the proton momentum distribution as Eq. 1.1

$$E_A\frac{d^3N_A}{d^3p_A} = B_A(E_p\frac{d^3N_p}{d^3p_p})^Z(E_n\frac{d^3N_n}{d^3p_n})^{A-Z} \tag{1.1}$$

where $E\frac{d^3N}{d^3p}$ is the invariant yield of nucleons or nuclei, A is the nuclear number of the produced nucleus and N, Z are the numbers of neutron and proton in the nucleus, respectively.

In the thermodynamic models, after the hadronization of the fireball (the collision reaction zone with high temperature and energy density), the grand canonical partition function Z for a hadronic resonance gas at temperature T is defined in the statistical mechanics as Eq. 1.2.

$$Z = \sum_n \langle n | e^{(H-\mu\hat{N})/T} | n \rangle \tag{1.2}$$

Here H is the Hamiltonian, μ is the chemical potential and $\hat{N}$ is the particle number operator. Coming from the partition function Z, the thermodynamic values pressure P, particle number N and entropy S can be calculated as the following.

$$P = T\frac{\partial \ln Z}{\partial V} \tag{1.3}$$

$$N = T\frac{\partial \ln Z}{\partial \mu} \tag{1.4}$$

$$S = \frac{\partial (T \ln Z)}{\partial T} \tag{1.5}$$

Here V is the volume of the system in which chemical equilibrium is reached. The energy E is given by

$$E = -PV + TS + \mu N \tag{1.6}$$

In the simple situation of an ideal gas of boson and fermions the partition function becomes

$$\ln Z = \pm\frac{gV}{2\pi^2}\int p^2 dp \ln(1 \mp e^{-\frac{E_i-\mu}{T}}) \tag{1.7}$$

Here, g is the spin degeneracy. E_i is the energy of the particle of species i and "±" is selected according to the quantum statistics for bosons and fermions, respectively. For the numbers of particles of a given species i, from Eq. 1.4 we can get

$$N = \frac{gV}{2\pi^2}\int \frac{p^2 dp}{e^{\frac{E_i p-\mu}{T}} \mp 1} \tag{1.8}$$

and thus for the differential multiplicity (particle's yield)

$$\frac{d^3N}{dp^3} = \frac{gV}{(2\pi)^3}\frac{1}{e^{\frac{E_i(p)-\mu}{T}} \mp 1} \tag{1.9}$$

In the coalescence models with classical statistics, if we apply Eq. 1.9 in the Boltzmann limit,

$$\frac{d^3N}{dp^3} = \frac{gV}{(2\pi)^3} e^{(-\frac{E-\mu}{T})} \tag{1.10}$$

to both the cluster and constituent nucleons and a cluster chemical potential of

$$\mu_A = N\mu_n + Z\mu_p \tag{1.11}$$

in a thermal and chemical equilibrated volume, we can conclude directly that

$$B_A = A\frac{2s_A+1}{2^A} R^N_{np} (\frac{(2\pi\hbar)^3}{mV})^{A-1} \tag{1.12}$$

Here R^N_{np} is the ratio of neutrons and protons in the source. s_A and m is spin of the cluster (d or ^3He) and the proton mass, respectively. Here, B_A depends on the source volume V as

$$B_A \propto (1/V)^{A-1} \tag{1.13}$$

Unlike the classical approaches, the quantum mechanical description can take the internal cluster structure and energy conservation into account. Scheibl and Heinz [7] incorporate in their coalescence model formulation a dynamically expanding source in both transverse and longitudinal direction, motivated by hydrodynamics. As they assume also a local thermal and chemical equilibrium, the coalescence parameter is in its form identical with the classical results in Eq. 1.12, modified only by a quantum mechanical correction factor $\langle C_A \rangle$ and a replacement of the source volume in coordinate space V by an effective volume V_{eff},

$$B_A = A\frac{2s_A+1}{2^A} \langle C_A \rangle \frac{V_{eff}(A, M_t)}{V_{eff}(1, m_t)} (\frac{(2\pi\hbar)^3}{m_t V_{eff}(1, m_t)})^{A-1} \tag{1.14}$$

Here M_t is the nuclei transverse mass which is related to the nucleon transverse mass as $M_t = Am_t$. The effective volume V_{eff} depends on the mass number A and the transverse momentum as a consequence of transverse collective flow. Using the similarity of coalescence and HBT, Scheibl and Heinz find an expression of the effective volume in term of HBT radii $R_\perp$ (R_{side}) and $R_\parallel$ (R_{long}) as

$$V_{eff}(A, M_t) = (\frac{2\pi}{A})^{3/2} R^2_\perp(m_t) R_\parallel(m_t) \tag{1.15}$$

At RHIC energy, STAR experiment has measured the $\bar{d}$ and $\overline{^3He}$ spectra at low p_T [11]. The particle identification was done by the charged tracks' ionization energy in the TPC detector. PHENIX experiment also measured the d and $\bar{d}$ spectra at intermediate p_T by using the TOF detectors [12]. At lower energy heavy-ion and $p+p$ colliders such as SPS, AGS and $Bevelac$, the light nuclei production has also been measured [90]. The coalescence parameter B2 is shown in Fig. 1.4. The results

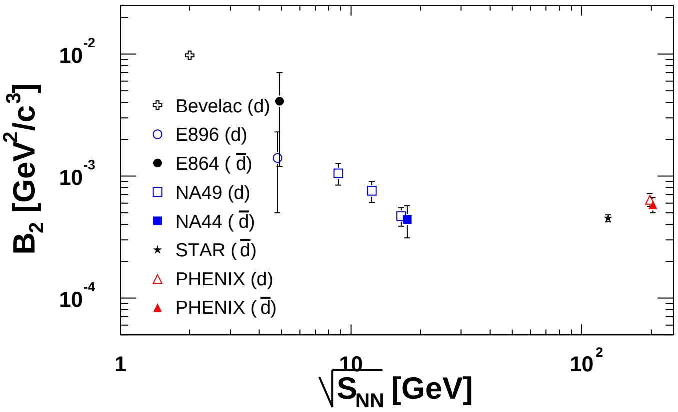

Figure 1.4: Comparison of the coalescence parameter for deuterons and anti-deuterons with other experiments at different values of $\sqrt{s_{NN}}$.

combined with the analyses in this thesis and other experiments will be discussed in Chapter 5 and 6.

As we know, hadrons at intermediate p_T mainly come from the coalescence of quarks. It directly results in the NQ scaling of the baryon and meson's elliptic flow parameter v_2 [13, 14], which is shown in Fig. 1.5. The light nuclei are mostly formed by the final-state coalescence, which happens at the moment of thermal freeze-out. Therefore, like the NQ scaling of the hadrons, one would predict the light nuclei v_2 follow the A scaling, where A is the atomic mass number of the nuclei. Thus, the light nuclei v_2 study, which has never be done before, is a good way to further understand the formation of nuclei.

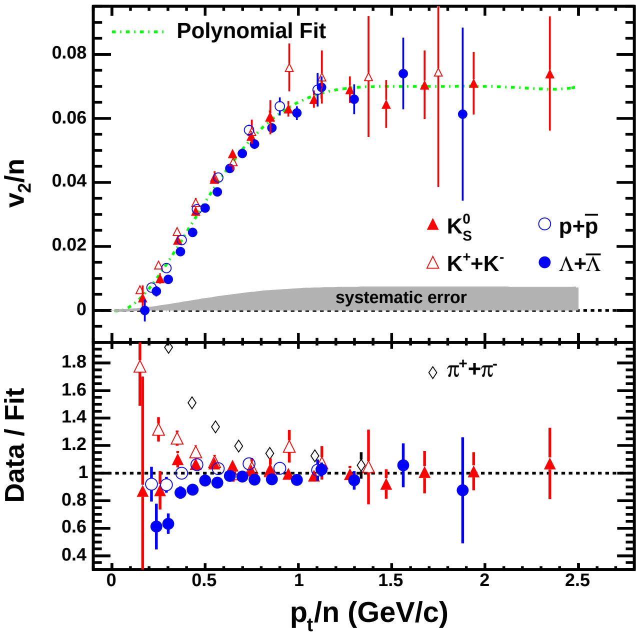

Figure 1.5: Top panel: Identified particle v_2 from minimum bias collisions. The vertical axis and horizontal axis have been scaled by the number of constituent quarks (n). A polynomial curve is fit to the data. The possible systematic error is indicated by the gray band. Bottom panel: The ratio of v_2/n to the fitted curve.

1.4 Source of meson and baron production

In LEP $e^+ + e^-$ experiments, DELPHI collaboration has measured the identified charged particle ($\pi^\pm$, $K^\pm$ and $p(\bar{p})$) spectra from two kinds of hadronic Z decays: quark jets and gluon jets [15]. Fig. 1.6 shows the ratios of the momentum spectra of identified hadrons in gluon and quark jets cases. It is clear that at high p_T ($p_T > 3\ GeV/c$), the $p(\bar{p})$ production is enhanced in the gluon jets case while $\pi^\pm$ production is not or even suppressed. This indicates when $p_T > 3\ GeV/c$, the $p(\bar{p})$ production is dominated by the gluon jets fragmentation while the quark jets fragmentation contributes more to the $\pi^\pm$ production.

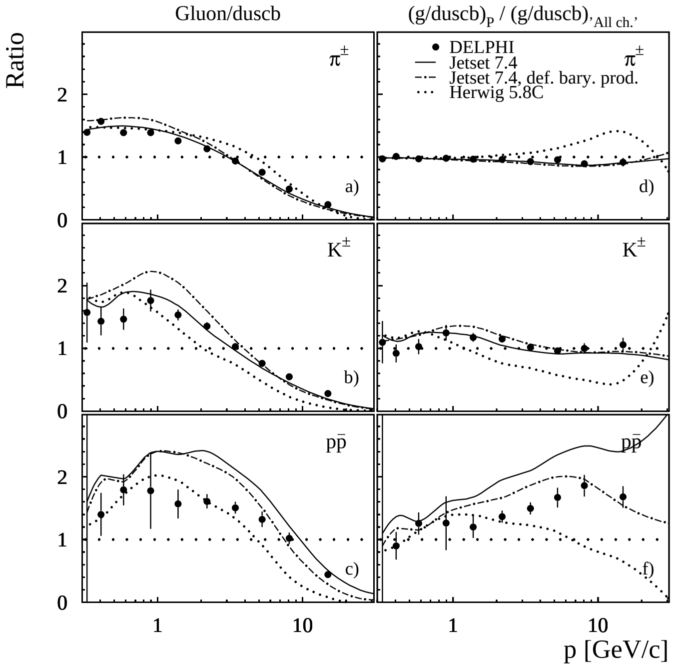

Figure 1.6: Ratios of the momentum spectra of identified hadrons in gluon and quark(duscb) jets of the hadronic Z decay events; Panel a-c: ratios of the spectra of pions, kaons, and protons in gluon jets to those in quark jets; Panel d-f: corresponding spectra normalized to the ratio gluon/quark for all charged particles. The predictions of the generator models JETSET, JETSET with default baryon production model and HERWIG are drawn as lines.

We can also study the baryon ($p(\bar{p})$) source by another method: P.J. Siemens, L.P. Csernai and F.Q. Wang introduced that one could access the baryon phase space density by measuring the ratio of $d(\bar{d})$ and $p(\bar{p})$ [16, 17, 18].

Eq. 1.16 is the definition of particle phase space density,

$$f(p,x) = \frac{dN}{dpdx} \tag{1.16}$$

which is Lorentz invariant. Consider identical particles in a small momentum cell $(p, p+dp)$, which occupy a spatial volume $V(p)$ in the particle rest frame. If these particles are uniformly distributed, then the spatial averaged phase space density is

$$\langle f(p) \rangle = \frac{E}{m} \frac{dN/dp}{V(p)} \tag{1.17}$$

where m is the particle rest mass and E/m is due to the Lorentz boost.

Instead of a uniform distribution in space, if we take a Gaussian form for the particle density profile, which is often used to extract source size parameters [19, 20, 21],

$$f(p,x) = \frac{E}{m} \frac{dN/dp}{(\sqrt{2\pi} R_G(p))^3} e^{-\frac{(x-x_0(p))^2}{2R_G^2(p)}} \tag{1.18}$$

then Eq. 1.17 becomes

$$\langle f(p) \rangle = \frac{E}{m} \frac{dN/dp}{(2\sqrt{\pi} R_G(p))^3} \tag{1.19}$$

Here R_G is a measure of the relative reparation of two particles close in momentum in the pair rest frame.

In the coalescence model with a Gaussian density profile,

$$R_G^3(p_p) = \frac{3}{4} \pi^{3/2} \frac{(\frac{E_p}{m_p} \frac{dN_p}{dp_p})^2}{(\frac{E_d}{m_d} \frac{dN_d}{dp_d})_{p_d = 2p_p}} \tag{1.20}$$

where the factor 3/4 comes from spin consideration, and subscripts “p” and “d” denote proton and deuteron, respectively. From Eq. 1.19 and 1.20, we obtain

$$\langle f(p_p) \rangle = \frac{4}{3(2\pi)^3} \frac{(\frac{E_d}{m_d} \frac{dN_d}{dN_d})_{p_d = 2p_p}}{\frac{E_p}{m_p} \frac{dN_p}{dN_p}} \tag{1.21}$$

where the neutron and proton differential cross section are assumed to be identical. Therefore, the p_T averaged proton phase space space density is

$$\langle f(y) \rangle = \frac{1}{6(2\pi)^3} \frac{(dN/dy)_d}{(dN/dy)_p} \tag{1.22}$$

The averaged over the whole phase space is

$$\langle f(y) \rangle = \frac{1}{6(2\pi)^3} \frac{N_d}{N_p} \tag{1.23}$$

Hence, with a series $d(\bar{d})$ and $p(\bar{p})$ measurements, we will be able to have a better understanding of the baryon phase space density and the source of baryon production. See Chapter 6 for detailed discussions.

1.5 Jet quenching and parton energy loss

In heavy-ion collisions, high p_T ($p_T \geq 5\ GeV/c$) particles are believed to be produced from the fragmentation of the energetic partons, which are created by the initial QCD hard scattering processes [22]. When energetic partons propagating the QGP, which is hot and dense, they lose energy. Therefore, these energetic particles can be used as unique probes by studying their interactions with the medium.

Recently, S. Wicks *et al.* have studied the parton energy loss with perturbative QCD [23].

Fig. 1.7 shows of the parton energy loss for deferent flavor of quarks. It is found that the light quarks lose more energy than heavy quarks due to the large mass effect [24, 25].

If the source geometry and density profile are taken into account [26], the partonic nuclear modification can be derived and compare with real data directly. Fig. 1.8 shows the partonic nuclear modification as a function of p_T. A strong color charge dependence can be seen clearly.

Experimentally, at high p_T, the suppression for charged hadron production was observed in Au+Au collisions at RHIC energy [27, 28]. The comparison of the spectra in Au+Au collisions through those in p+p collisions, scaled by the number of binary nucleon nucleon collisions is the nuclear modification factor R_{AA}.

$$R_{AA}(p_T) = \frac{d^2N^{AA}/dp_T d\eta}{T_{AA} d^2\sigma^{NN}/dp_T d\eta} \tag{1.24}$$

Here $T_{AA} = \langle N_{\rm bin} \rangle / \sigma_{\rm inel}^{NN}$ accounts for the collision geometry, averaged over the event centrality class. $\langle N_{\rm bin} \rangle$, the equivalent number of binary NN collisions, is calculated

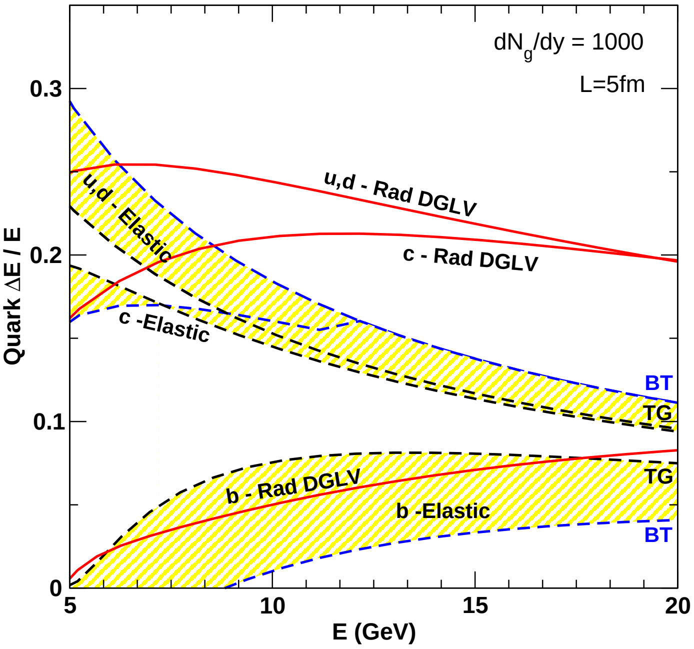

Figure 1.7: Average $\Delta E/E$ for u, c, b quarks as a function of E. A Bjorken expanding QGP with path length $L = 5\ fm$ and initial density fixed by $dN_g/dy = 1000$ is assumed. The curves are computed with the coupling $\alpha_s = 0.3$ held fixed. For Debye mass $\mu_D \propto (dN_g/dy)^{(1/3)}$, the gluon mass is $\mu_D/\sqrt{2}$, the light quark mass is $\mu_D/2$, the charm mass is 1.2 GeV, and the bottom mass is 4.75 GeV. Radiative DGLV first order energy loss is compared to elastic parton energy loss (in TG or BT approximations). The yellow bands provide an indication of theoretical uncertainties in the leading log approximation to the elastic energy loss.

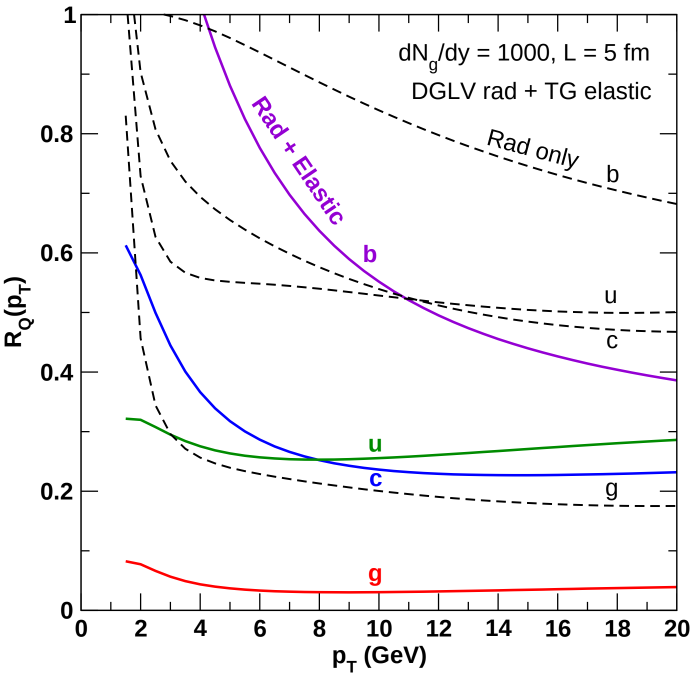

Figure 1.8: Partonic nuclear modification for g, u, c, b as a function of p_T for fixed L=5 fm path length and $dN_g/dy = 1000$. Dashed curves include only radiative energy loss, while solid curves include elastic energy loss as well.

using a Glauber model [29]. The R_{AA} is an experimental variable. The high p_T hadron suppression in central Au+Au collisions can also be investigated by comparing the hadron spectra in central and peripheral Au+Au collisions. That's what we called R_{CP}. R_{CP} is defined as

$$R_{CP} = \frac{\langle N_{\text{bin}}^{\text{peripheral}} \rangle d^2N^{\text{central}}/dp_T d\eta}{\langle N_{\text{bin}}^{\text{central}} \rangle d^2N^{\text{peripheral}}/dp_T d\eta}. \tag{1.25}$$

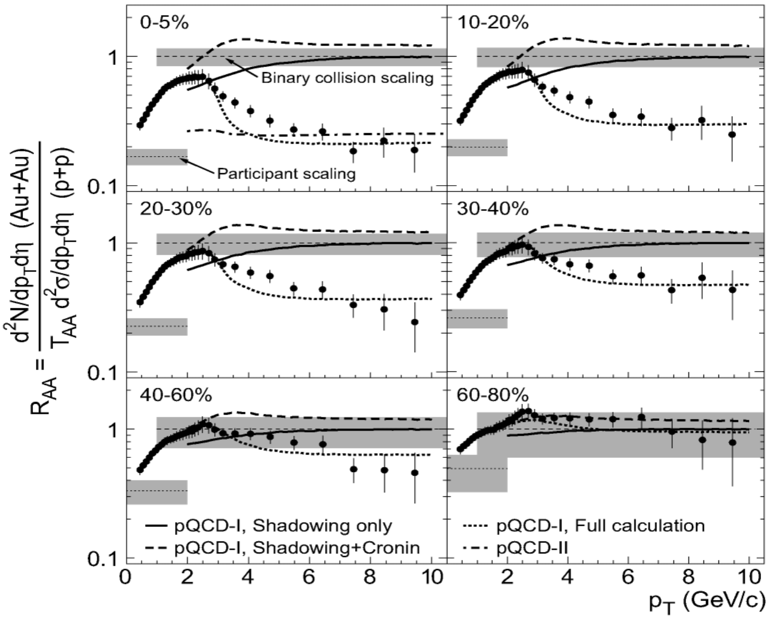

Figure 1.9: $R_{AA}(p_T)$ of inclusive charged hadron for various centrality bins. Figure is taken from Ref. [27].

Fig. 1.9 shows the R_{AA} of inclusive charged hadron for various centrality bins in central Au+Au collisions at $\sqrt{s_{NN}} = 200\ GeV$. Fig. 1.10 shows the R_{AA} of two mesons (π^0, η) and the direct photon in central Au+Au collisions at $\sqrt{s_{NN}} = 200\ GeV$. At high p_T, the strong suppression can be seen for hadrons. The suppression is due to the energetic parton loses energy when they propagating the dense medium. Since photons don't involve in the strong interaction, no suppression is found in the data.

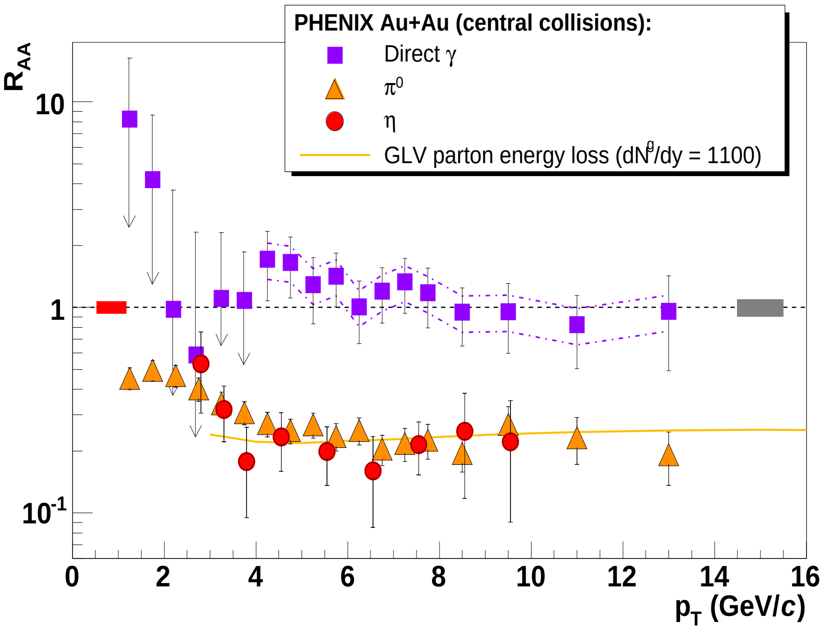

Figure 1.10: $R_{AA}(p_T)$ measured in central Au+Au at $\sqrt{s_{NN}} = 200\ GeV$ for η, π^0 and direct γ. Figure is taken from Ref. [28].

As we mentioned before, high p_T baryon and meson have difference partonic source. Hence, to study the identified particle spectra on large transverse momentum will lead us to a better understanding of the color charge dependence of partonic energy loss.

Chapter 2

Experimental facilities

2.1 RHIC accelerator

The Relativistic Heavy Ion Collider (RHIC) at Brookhaven National Lab (BNL) is the first hadron accelerator and collider consisting of two independent ring. It is designed to operate at high collision luminosity over a wide range of beam energies and particle species ranging from polarized proton to heavy ion [30, 31], where the top energy of the colliding center-of-mass energy per nucleon-nucleon pair is $\sqrt{s_{NN}}$ = 200 GeV. The RHIC facility consists of two super-conducting magnets, each with a circumference of 3.8 km, which focus and guide the beams.

Figure 2.1 shows the BNL accelerator complex including the accelerators used to bring the gold ions up to RHIC injection energy. In the first, gold ions are accelerated to 15 MeV/nucleon in the Tandem Van de Graaff facility. Then the beam is transferred to the Booster Synchrotron and accelerated to 95 MeV/nucleon through the Tandem-to-Booster line. Then the gold ions are transferred to the Alternating Gradient Synchrotron (AGS) and accelerated to 10.8 GeV/nucleon. Finally they are injected to RHIC and accelerated to the collision energy 100 GeV/nucleon.

RHIC's 3.8 km ring has six intersection points where its two rings of accelerating magnets cross, allowing the particle beams to collide. The collisions produce the fleeting signals that, when captured by one of RHIC's experimental detectors, provide physicists with information about the most fundamental workings of nature. If

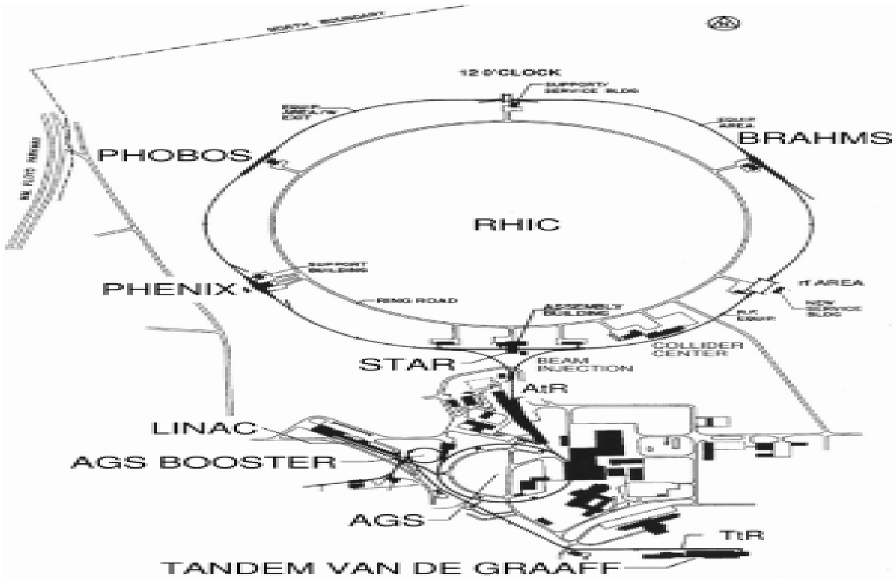

Figure 2.1: A diagram of the Brookhaven National Laboratory collider complex including the accelerators that bring the nuclear ions up to RHIC injection energy (10.8 GeV/nucleon for ^{197}Au). Figure is taken from [32, 33].

RHIC's ring is thought of as a clock face, the four current experiments are at 6 o'clock (STAR), 8 o'clock (PHENIX), 10 o'clock (PHOBOS) and 2 o'clock (BRAHMS). There are two additional intersection points at 12 and 4 o'clock where future experiments may be placed [30].

2.2 STAR detector

The Solenoidal Tracker at RHIC (STAR) is one of the two large detector systems constructed at the Relativistic Heavy Ion Collider (RHIC) at Brookhaven National Laboratory. STAR was constructed to investigate the behavior of strongly interacting matter at high energy density and to search for signatures of quark-gluon plasma (QGP) formation. Key features of the nuclear environment at RHIC are a large number of produced particles (up to approximately one thousand per unit pseudorapidity) and high momentum particles from hard parton-parton scattering. STAR can measure many observables simultaneously to study signatures of a possible QGP

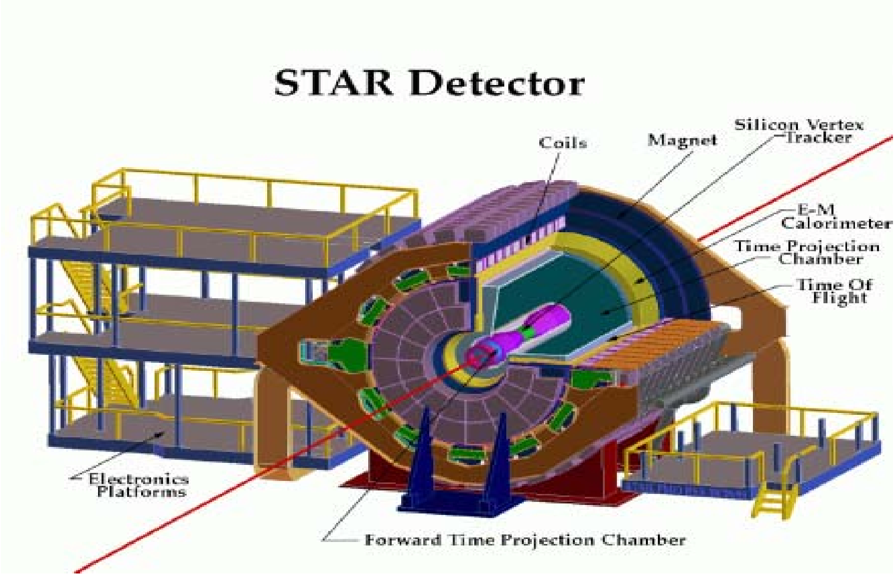

Figure 2.2: Perspective view of the STAR detector, with a cutaway for viewing inner detector systems. Figure is taken from [34].

phase transition and to understand the space-time evolution of the collision process in ultra-relativistic heavy ion collisions. The goal is to obtain a fundamental understanding of the microscopic structure of these hadronic interactions at high energy densities. In order to accomplish this, STAR was designed primarily for measurements of hadron production over a large solid angle, featuring detector systems for high precision tracking, momentum analysis, and particle identification at the center of mass (c.m.) rapidity. The large acceptance of STAR makes it particularly well suited for event-by-event characterizations of heavy ion collisions and for the detection of hadron jets [34].

The layout of the STAR experiment [35] is shown in Fig. 2.2. A cutaway side view of the STAR detector as configured for the RHIC 2001 run is displayed in Fig. 2.3. A room temperature solenoidal magnet [36] with a maximum magnetic field of 0.5 T provides a uniform magnetic field for charged particle momentum analysis. Charged particle tracking close to the interaction region is accomplished by a Silicon Vertex Tracker [37] (SVT). The Silicon Drift Detectors [38] (SDD) installed after 2001 is also for the inner tracking. The silicon detectors cover a pseudo-rapidity range $\mid \eta \mid \leq 1$

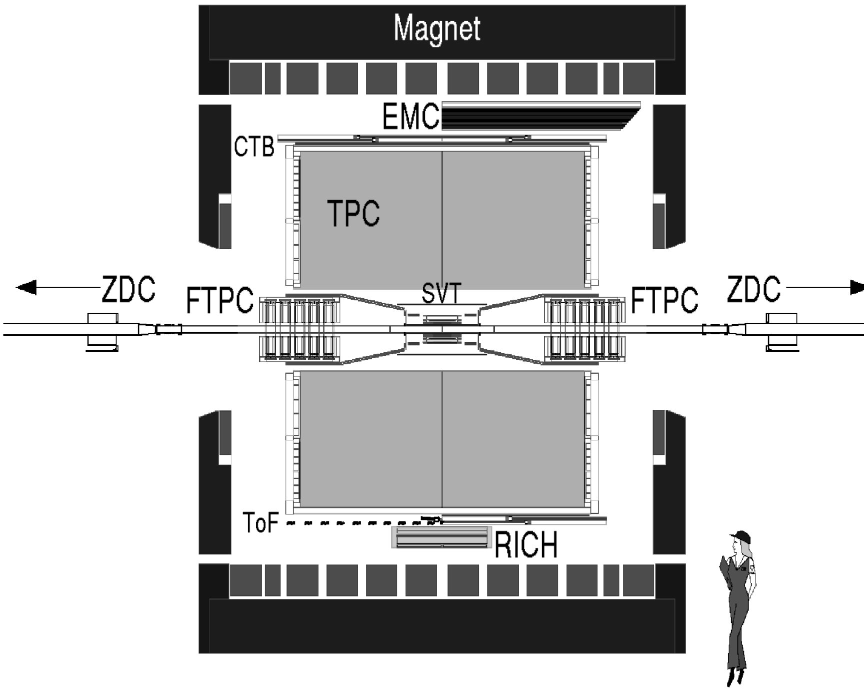

Figure 2.3: Cutaway side view of the STAR detector as configured in 2001. Figure is taken from [34].

with complete azimuthal symmetry ($\Delta\phi = 2\pi$). Silicon tracking close to the interaction allows precision localization of the primary interaction vertex and identification of secondary vertices from weak decays of, for example, Λ, Ξ, and Ω. A large volume Time Projection Chamber [39, 40] (TPC) for charged particle tracking and particle identification is located at a radial distance from 50 to 200 cm from the beam axis. The TPC is 4 meters long and it covers a pseudo-rapidity range $\mid \eta \mid \leq 1.8$ for tracking with complete azimuthal symmetry ($\Delta\phi = 2\pi$). Both the SVT and TPC contribute to particle identification using ionization energy loss, with an anticipated combined energy loss resolution (dE/dx) of 7 % (σ). The momentum resolution of the SVT and TPC reach a value of $\delta\mathrm{p}/\mathrm{p} = 0.02$ for a majority of the tracks in the TPC. The $\delta\mathrm{p}/\mathrm{p}$ resolution improves as the number of hit points along the track increases and as the particle's momentum decreases, as expected [34].

To extend the tracking to the forward region, a radial-drift TPC (FTPC) [41] is installed covering $2.5 <| \eta |< 4$, also with complete azimuthal coverage and symmetry. To extend the particle identification in STAR to larger momenta over a small solid angle for identified single-particle spectra at mid-rapidity, a ring imaging Cherenkov detector [42] covering $| \eta |< 0.3$ and $\Delta\phi = 0.11\pi$, and a time-of-flight patch (TOFp) [43] covering $-1 < \eta < 0$ and $\Delta\phi = 0.04\pi$ (as shown in Fig. 2.3) was installed at STAR in 2001 [34]. In 2003, a time-of-flight tray (TOFr) based on multi-gap resistive plate chamber (MRPC) technology [44] was installed in STAR detector, covering $-1 < \eta < 0$ and $\Delta\phi = \pi/30$. For the time-of-flight system, the Pseudo-Vertex Position Detectors (pVPD) was installed as the start-timing detector, which was 5.4 m away from TPC center and covers $4.4 < |\eta| < 4.9$ with the azimuthal coverage 19% [43] in 2003.

The fast detectors that provide input to the trigger system are a central trigger barrel (CTB) at $|\eta| < 1$ and two zero-degree calorimeters (ZDC) located in the forward directions at $\theta < 2$ mrad. The CTB surrounds the outer cylinder of the TPC, and triggers on the flux of charged particles in the mid-rapidity region. The ZDCs are used for determining the energy in neutral particles remaining in the forward directions [34]. A minimum bias trigger was obtained by selecting events with a pulse height larger than that of one neutron in each of the forward ZDCs, which corresponds to 95 percent of the geometrical cross section [34].

2.3 Time projection chamber

TPC is the main detector of STAR [40]. Consisting of a 4.2 m long cylinder with 4.0 m in diameter, it is the largest single TPC in the world. The cylinder is concentric with the beam pipe, and the inner and outer radii of the active volume are 0.5 m and 2.0 m, respectively. It can measure charged particles within momentum $0.15 < p_T/(\mathrm{GeV}/c) < 30$ (0.075 GeV/c low limit for 0.25 T). The TPC covers the full region of azimuth ($0 < \phi < 2\pi$) and covers the pseodurapidity range of $|\eta| < 2$ for inner radius and $|\eta| < 1$ for outer radius. Fig. 2.4 shows a cutaway view of the structure of the TPC.

The TPC is divided into two parts by the central membrane. It is typically held

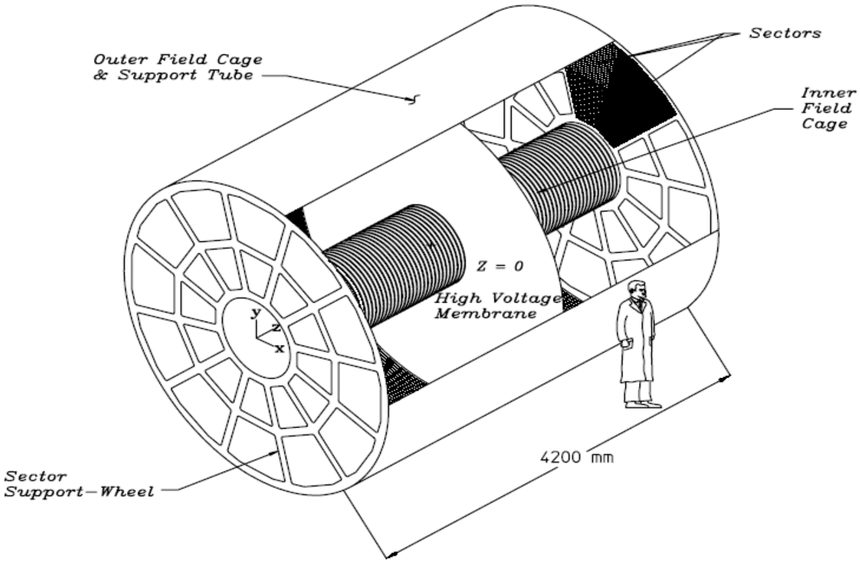

Figure 2.4: Cutaway view of the TPC detector at STAR.

at 28 kV high voltage. A chain of 183 resistors and equipotential rings along the inner and outer field cage create a uniform drift filed (~ 135 V/cm) from the central membrane to the ground planes where anode wires and pad planes are organized into 12 sectors for each sub-volume of the TPC. The working gas of the TPC is two gas mixture – P10 (Ar 90% + CH_4 10%) regulated at 2 mbar above the atmospheric pressure. The electron drift velocity in P10 is relatively fast, ~ 5.45 cm/μs at 130 V/cm drift field. The gas mixture must satisfy multiple requirements and the gas gains are ~ 3770 and ~ 1230 for the inner and outer sectors working at normal anode voltages (1170 V for inner and 1390 V for outer), respectively. Each readout plane is instrumented with a thin *Multi-Wire Proportional Chamber* (MWPC) together with a pad chamber readout. Each pad plane is also divided into inner and outer sub-sectors, while the inner sub-sector is designed to handle high track density near collision vertex. 136,608 readout pads provide (x, y) coordinate information, while z coordinate is provided by 512 time buckets and the drift velocity. Typical resolution is $\sim 0.5 - 1.0$ mm.

When charged particles traverse the TPC, they liberate the electrons from the

TPC gas due to the ionization energy loss (dE/dx). These electrons are drifted towards the end cap planes of the TPC. There the signal induced on a readout pad is amplified and integrated by a circuit containing a pre-amplifier and a shaper. Then it is digitalized and then transmitted over a set of optical fibers to STAR *Data AcQuisition system* (DAQ).

The TPC reconstruction process begins by the 3D coordinate space points finding. This step results in a collection of points reported in global Cartesian coordinates. The *Timing Projection chamber Tracker* (TPT) algorithm is then used to reconstruct tracks by helical trajectory fit. The resulted track collection from the TPC is combined with any other available tracking detector reconstruction results and then refit by application of a Kalman filter routine – a complete and robust statistical treatment. The primary collision vertex is then reconstructed from these global tracks and a refit on these tracks with the *distance of closest approach* (*dca*) less the 3 cm is preformed by a constrained Kalman fit that forces the track to originate from the primary vertex. The primary vertex resolution is $\sim 350\ \mu$m with more than 1000 tracks. The refit results are stored as primary tracks collection in the container. The reconstruction efficiency including the detector acceptance for primary tracks depends on the particle type, track quality cuts, p_T, track multiplicity *etc.* The typical value for the primary pions with $N_{fit} > 24$ and $|\eta| < 0.7$, $dca < 3.0$ cm is approximate constant at $p_T > 0.4$ GeV/c: $>\sim 90\%$ for Au+Au peripheral collisions and $\sim 80\%$ for central collisions, respectively.

2.4 Time of flight

STAR has proposed the full barrel *Time-Of-Flight* (TOF) detector upgrade based on the *Multi-gap Resistive Plate Chamber* (MRPC) technology in the coming future. The TOFp detector (a prototype based on scintillator technology) was installed since Run II [43]. It replaced one of CTB trays, covering $-1 < \eta < 0$, and $\pi/30$ in azimuth. It contains 41 scintillator slats with the signal read out by *Photo Multiplier Tubes* (PMTs). The resolution of TOFp is about ~ 85 ps in Au+Au collisions. However, due to the significant higher cost by the PMTs, this design will not be used in the

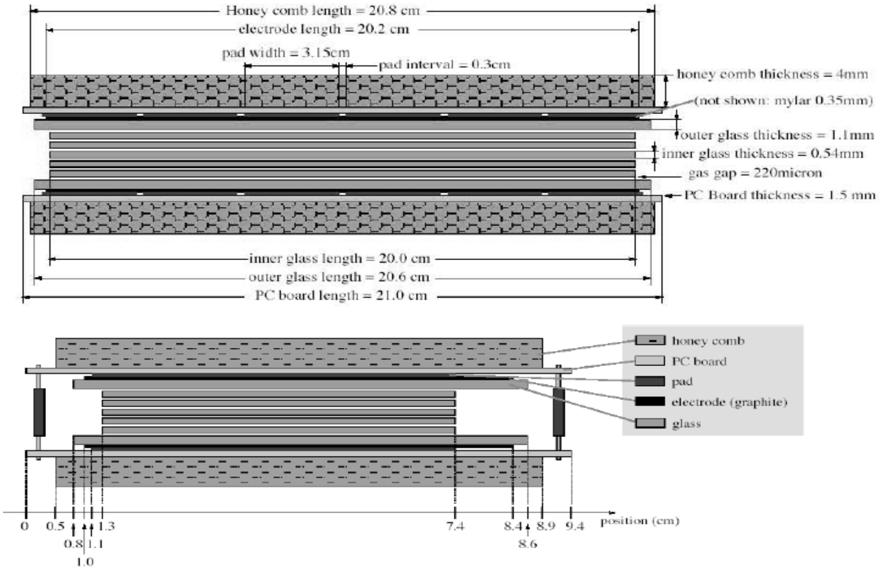

Figure 2.5: Two-side view of a MRPC module [44].

full TOF upgrade.

In Run III and Run IV, new prototypes of TOF detector based on MRPC (TOFr) were installed. Each also replaced one CTB tray, covering $-1 < \eta < 0$ and $\pi/30$ in azimuth too. In Run III, 28 MRPC modules were installed in the tray and 12 of them were equipped with electronics, corresponding to $\sim 0.3\%$ of the TPC acceptance [45]. In Run IV, 24 modules were installed in a new tray and the tray was put in the same position in STAR as Run III (but slightly global z position shift), but only 12 modules were equipped with valid electronics, which means the acceptance in Run IV was roughly similar to that in Run III.

Two pVPDs were installed as well since Run II to provide a starting time for TOF detectors, each staying 5.4 m away from the TPC center along the beam line [43]. Each pVPD consists of three detecting element tubes covering $\sim$ 19% of the total solid angle in $4.43 < |\eta| < 4.94$. Due to different multiplicities, the effective timing resolution of total starting time is 25 ps, 85 ps and 140 ps for 200 GeV Au+Au, d+Au and p+p collisions, respectively.

MRPC technology was first developed by the CERN ALICE group. Fig. 2.5 shows the two side views (long edge view on top and short edge view on bottom) of an MRPC module appropriate for STAR [44]. An MRPC basically consists a stack of resistive plates with a series of uniform gas gaps. It works in avalanch mode. Electrodes are applied to the outer surface of the outer plates. With a strong electric field applied on, the internal plates are left electrically floating and they will keep the correct voltage due to the flow of electrons and ions created in avalanches. There are six read-out strips on each module in this design. The first beam test for 6-gap MRPCs at CERN PS-T10 facility with $p_{lab} = 7$ GeV/c pions beam resulted in a ~ 65 ps timing resolution with more than 95% detecting efficiency and the module is capable of working at high event rate (500 Hz/cm^2) [44]. These modules were then assembled in a prototype TOF tray and tested in the AGS radiation area. Similar resolution was obtained. In RHIC Run III and Run IV, the MRPC modules in TOFr trays installed in the STAR detector were applied on the high voltage of 14 kV and with the working gas of 95% freon and 5% iso-butane. The charged particle detecting efficiency is $> 95\%$ at high voltage plateau.

TOF system calibrations include the start time calibration from pVPDs and TOFr/TOFp flight time calibration. The main sources need to be considered are global time offset due to different electronics delays, the correlation between the amplitude and the timing signals, the correlation between the hit position and the timing signals *etc.* Detailed calibrations on TOF systems can be found in Ref [47, 45].

Chapter 3

Data analysis

3.1 Data set

In this thesis, the results presented are based on the data taken in RHIC run IV Au+Au collisions at $\sqrt{s_{NN}} = 200\,GeV$. There are about 25 million minBias triggered events and 24 million central triggered events taken in this run. Among them, there are about 16 million minBias triggered events and 15 million central triggered events have TOF information.

3.2 Hadron PID

In STAR experiment, TPC is the main detector for tracking and identifying charged particles. For stable charged hadrons, the TPC provides π/K (π+K/p) identification up to $p_T \simeq 0.7$ (1.1) GeV/c by the ionization energy loss (dE/dx) as usually been quoted and presented in the previous physics analysis [48]. Direct particle identification (PID) capability for stable hadrons can be further enhanced by the proposed TOF. A TOF system with a time resolution of $\lesssim$ 100 ps at STAR is able to identify π/K (π+K/p) up to $p_T \simeq 1.6$ (3.0) GeV/c.

Fig. 3.1 shows the TPC dE/dx measurement as a function of momentum. Fig. 3.2 shows the TOF measurements of $1/\beta$ as a function of p_T. The tracks quality cut is listed in Table. 3.1.

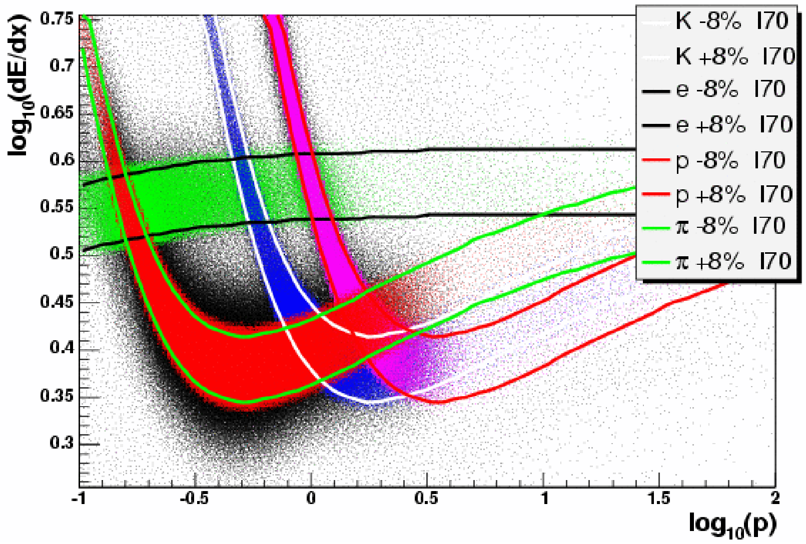

Figure 3.1: Distribution of $log_{10}(dE/dx)$ as a function of $log_{10}(p)$ for charged particles. The units of dE/dx and momentum (p) are keV/cm and GeV/c, respectively. The color bands denote within $\pm 1\sigma$ the dE/dx resolution. *I70* is a version code for Bichsel's prediction in STAR standard library.

3.2.1 PID at low p_T

At low p_T region ($p_T < 1.1\ GeV/c$), after dE/dx selection ($|n\sigma| < 2$), the raw yields of π and p ($\bar{p}$) can be directly counted. Fig. 3.3 shows the m^2 distributions for π^- and $\bar{p}$ at $0.7 < p_T < 0.8\ GeV/c$. $n\sigma$ is the normalized dE/dx and it is defined by Eq. 3.1, where X, Y can be $e^{\pm}, \pi^{\pm}, K^{\pm}$ or $p(\bar{p})$. B_X is the expected mean dE/dx of a particle X, and σ_X is the dE/dx resolution of TPC.

$$n\sigma_X^Y = \frac{log((dE/dx)_Y/B_X)}{\sigma_X} \tag{3.1}$$

Table 3.1: Tracks quality cuts for TOF

nFitPts	> 15
η	(-1, 0)
global dca (cm)	(0.0, 3.0)
TOF ADC (chn)	> 30

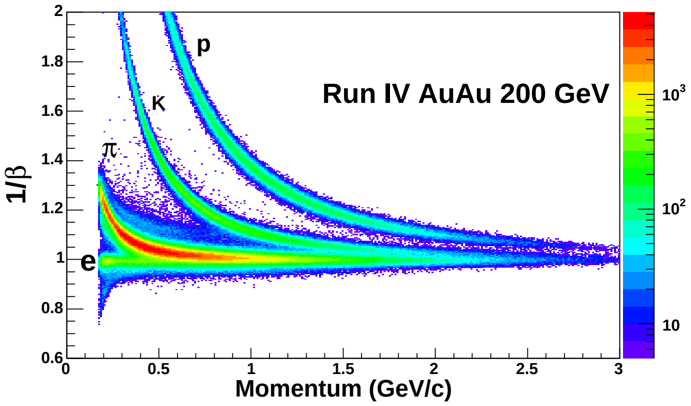

Figure 3.2: $1/\beta$ as a function of p_T measured by Time of Flight.

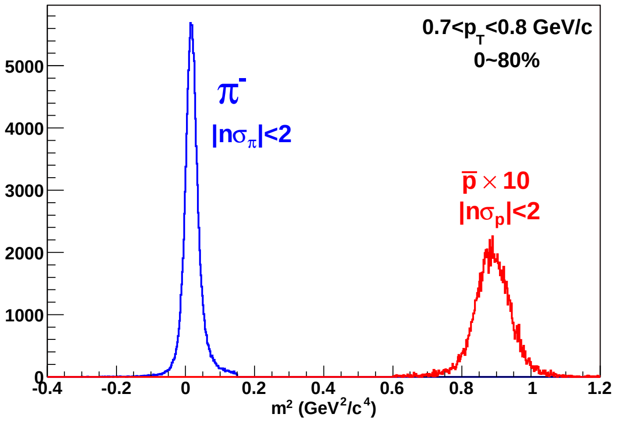

Figure 3.3: m^2 distributions after dE/dx selections at low p_T region.

3.2.2 PID at intermediate p_T

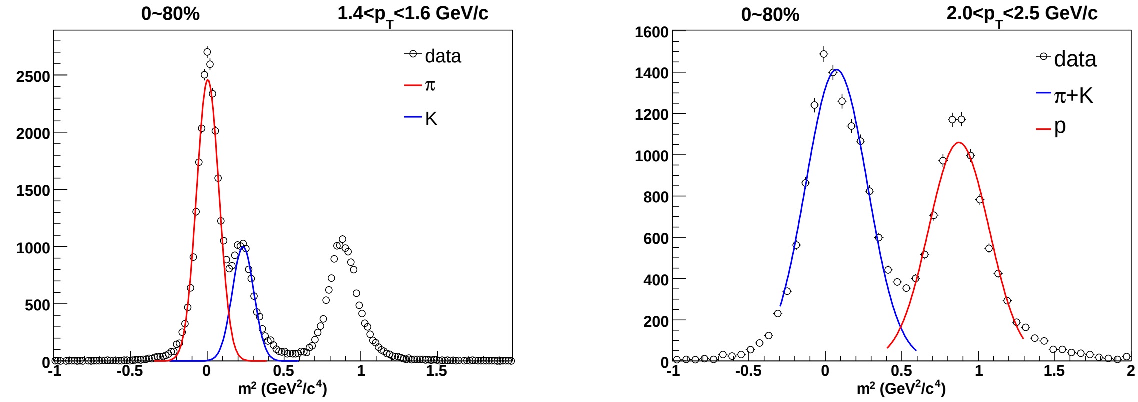

Figure 3.4: Two Gaussian fit for m^2 distributions after dE/dx selections at intermediate p_T region. The left panel is for pion and the right panel is for proton.

At intermediate p_T region ($1.1 < p_T < 4.0\ GeV/c$), the m^2 distribution of π, K and p ($\bar{p}$) will merge together. In this situation, we can fit m^2 distributions with Gaussian functions to derive the raw yields of π, K and p ($\bar{p}$). Fig. 3.4 shows how the m^2 distributions are fit with Gaussian functions.

However, the real shape of m^2 distributions for those particles are not really Gaussian. Fitting them with Gaussian functions will bring more systematic uncertainties. To get a better results, we use the predicted m^2 distributions to fit the total m^2 distribution instead of using Gaussian functions. This method is described as the following text.

First of all, it is assumed that the TOF detectors' responds to tracks are similar for different momenta and different particle tracks at $p_T \geq 1.0\ GeV/c$. At low p_T region, where TPC can identify particles by dE/dx very well, the momentum (p) and the track length (l) resolution is good. We can calculate the particle's "real" time of flight (t_{TPC}) by TPC information only. At the same time, TOF detectors also have a measurement on time of flight (t_{TOF}). Therefore, the difference between two times ($\Delta t = t_{TOF} - t_{TPC}$) reflects the behavior of TOF detectors' response to the matched tracks. The Δt distribution is shown in Fig. 3.5.

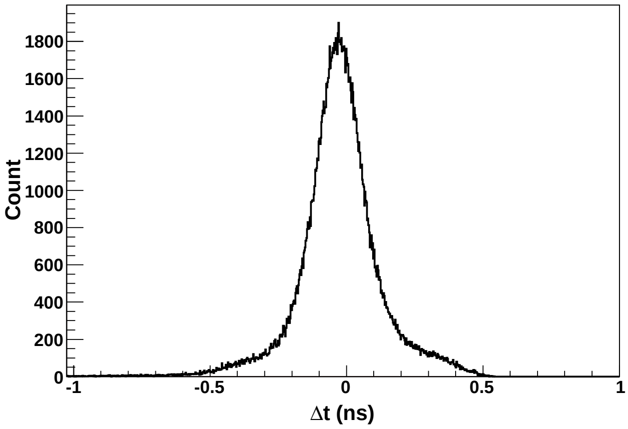

Figure 3.5: Δt distributions for TOF detectors.

At Intermediate p_T region, we can use the Δt distribution to simulate TOF detectors behavior. With a given momentum (p) and the track length (l), for a known particle type (m_0), the real time of flight (t_0) can be calculated by Eq. 3.2, where c is the speed of light. The simulated time of flight (t_{simu}) measured by TOF will be $t_0 + t_{random}$, here t_{random} is a random time shift generated based on the Δt distribution, which describes the TOF detectors response behavior. The predicted m^2 distributions can be determined, either.

$$t_0 = \frac{l\sqrt{p^2 + m_0^2}}{cp} \tag{3.2}$$

Fig. 3.6 shows the predicted m^2 distributions for π, K and p ($\bar{p}$) in different p_T bins.

We use the least χ^2 method to fit the real data m^2 distribution with the predicted particle m^2 distributions. In the mean time, we also fit the $n\sigma$ distributions measured from TPC dE/dx with 3-gaussian functions to further constrain the results. Fig. 3.7 shows a typical case of fit for the predicted m^2 method.

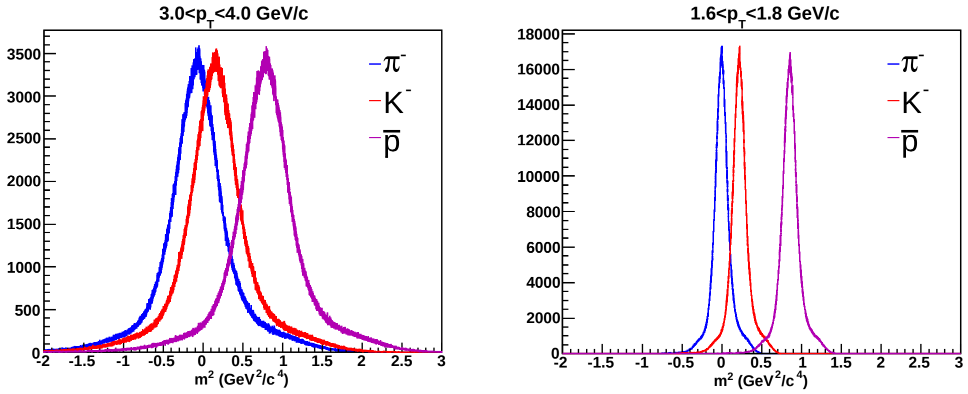

Figure 3.6: Predicted m^2 distributions in different p_T bins.

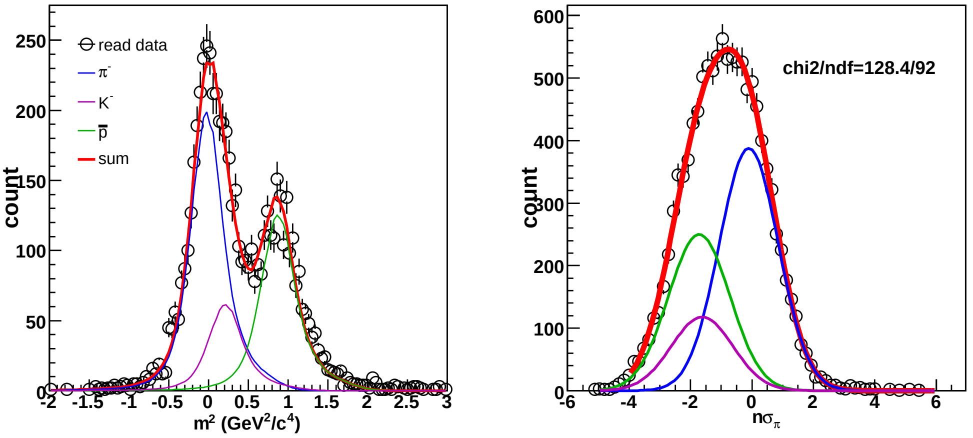

Figure 3.7: Left panel: real data m^2 distribution fit by predicted m^2 distributions. Right panel: $n\sigma$ distributions fit by 3-Gaussian functions.

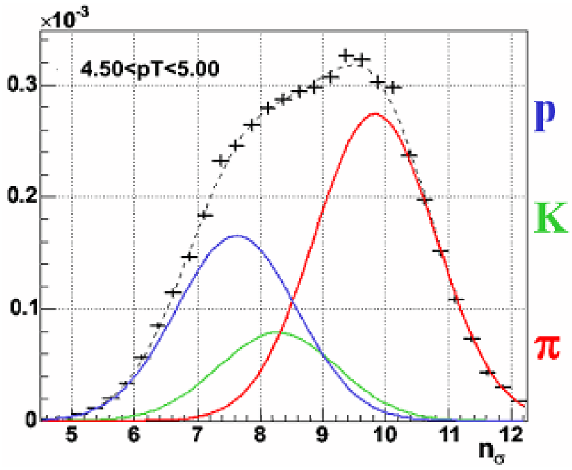

Figure 3.8: dE/dx distribution normalized by pion dE/dx at $4 < p_T < 4.5$ GeV/c

3.2.3 PID at high p_T

At high p_T ($p_T > 3\ GeV/c$), as shown in Fig. 3.1, there is a difference of about 15% in the dE/dx between pions and kaons due to the pion relativistic rise of the ionization energy loss. The difference between that of pions and (anti-)protons is even larger. This allows us to identify pions from other hadrons at this p_T range by the TPC alone at 2σ level. Fig. 3.8 shows the $n\sigma_\pi$ distributions fit by 3-Gaussian functions. Good K_s^0 measurements can also help to constrain p and $\bar{p}$ yields at high p_T. This method is named as relativistic dE/dx (rdE/dx) method. Detailed discussions can be found at Ref. [44].

3.3 Efficiencies and corrections

3.3.1 TPC tracking efficiency

TPC tracking efficiency is studied by Monte Carlo simulations. The simulated $\pi^\pm$, p and $\bar{p}$ are generated using a flat p_T and a flat y distribution and pass through GSTAR [49] (the framework software package to run the STAR detector simulation using GEANT [50, 51]) and TRS (the TPC Response Simulator [49]). The simulated

$\pi^{\pm}$, p and $\bar{p}$ are then combined with a real raw event and we call this combined event a simulated event. This simulated event is then passed through the standard STAR reconstruction chain and we call this event after reconstruction a reconstructed event. The reconstructed information of those particles in the reconstructed event is then associated with the Monte-Carlo information in the simulated event. And then we get the total number of simulated $\pi^{\pm}$, p and $\bar{p}$ from simulated events in a certain transverse momentum bin. Also we can get the total number of associated tracks in the reconstructed events in this transverse momentum bin [33]. In the end, take the ratio of the number of associated $\pi^{\pm}$, p and $\bar{p}$ over the number of simulated $\pi^{\pm}$, p and $\bar{p}$ and this ratio is the TPC reconstruction efficiency for a certain transverse momentum bin in the mid-rapidity range. Fig. 3.9 and Fig. 3.10 show the TPC reconstruction efficiency of $\pi^{\pm}$, p and $\bar{p}$ as a function of p_T in different centrality bins.

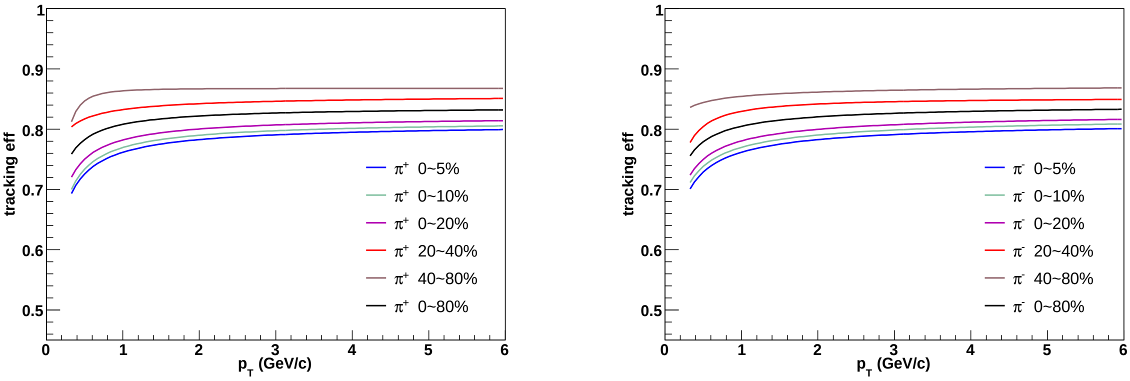

Figure 3.9: TPC reconstruction efficiency as a function of p_T. The left panel is for π^+ and the right panel is for π^-.

3.3.2 TOF matching efficiency

The matching efficiency from TPC to TOF are studied in real data and the the definition is shown in Eq. 3.3. The tracks selection is the necessary tracks quality cuts and $|n\sigma| < 2$ for different particles.

$$Matching\ eff = \frac{the\ Number\ of\ Tof\ Matched\ Tracks}{the\ Number\ of\ TPC\ Tracks} \tag{3.3}$$

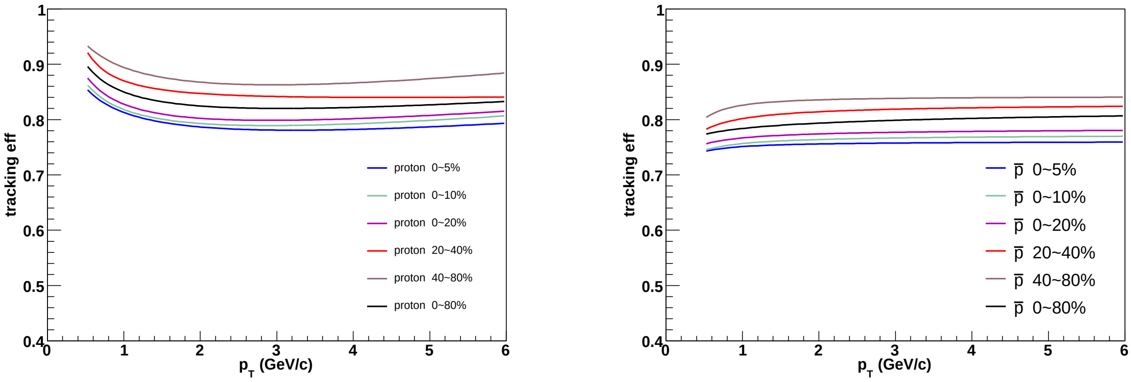

Figure 3.10: TPC reconstruction efficiency as a function of p_T. The left panel is for p and the right panel is for $\bar{p}$.

Therefore, the matching efficiency includes the TOF detectors acceptance, the response efficiency and the material absorption effect. Fig. 3.11 and Fig. 3.12 show the TOF matching efficiency of $\pi^{\pm}$, p and $\bar{p}$ as a function of p_T in different centrality bins.

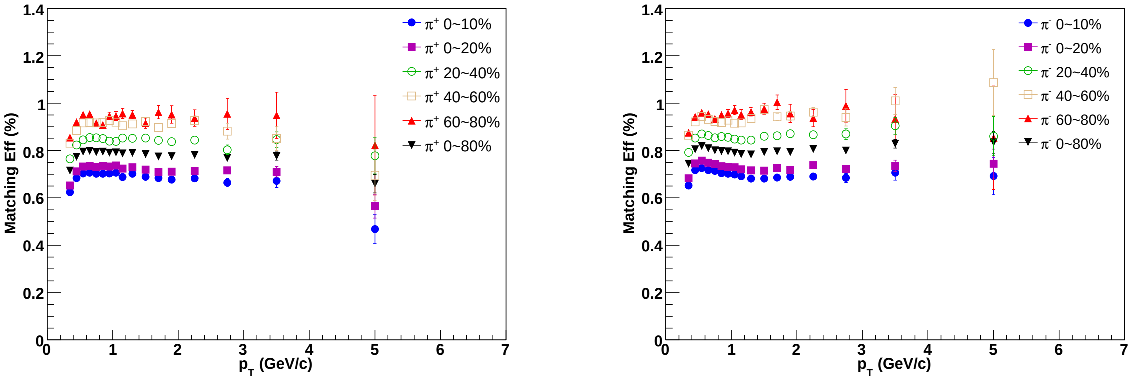

Figure 3.11: TOF matching efficiency as a function of p_T. The left panel is for π^+ and the right panel is for π^-.

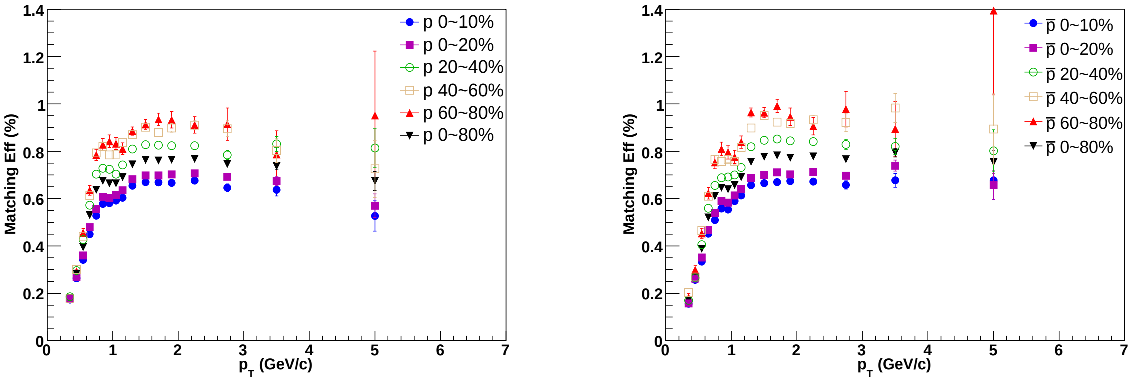

Figure 3.12: TOF matching efficiency as a function of p_T. The left panel is for p and the right panel is for $\bar{p}$.

3.3.3 Beam pipe scattering effect correction

For low p_T proton, there is some scattering contribution which comes from the beam pipe interaction. Obviously this effect has no contribution to the anti-particles like $\bar{p}$. The protons which come from the beam pipe scattering have large dca. Therefore, we can use Eq. 3.4 to correct the low p_T proton spectra.

$$p\ yield = \frac{\bar{p}\ yield|_{dca<3cm}}{\bar{p}\ yield|_{dca<1cm}} \times p\ yield|_{dca<1cm} \tag{3.4}$$

3.4 Feed-down correction

3.4.1 Feed-down correction for pions

Weak-decay feed-down (e.g. $K^0_S \rightarrow \pi^+\pi^-$) to the pion spectra is calculated using the measured K^0_S and Λ spectra [13] and GEANT simulation. The feed-down contribution is subtracted from the pion spectra and found to be $\sim 12\%$ at $p_T = 0.35\ GeV/c$, decreasing to $\sim 5\%$ for $p_T \geq 1\ GeV/c$.

3.4.2 Feed-down correction for protons and anti-protons

The p and $\bar{p}$ feed-down corrections are estimated using the Λ spectra from Ref. [13] with a full simulation of decay, detection efficiency, and momentum resolution. The measured Λ spectra are extrapolated to high p_T assuming $\Lambda/p = 0.2$ at $p_T = 10$ GeV/c. The Σ^+/Λ ratio is assumed to be 0.35 [52], independent of p_T. The systematic uncertainty on the correction is calculated from the statistical and systematic uncertainties on the inclusive proton and Λ measurements, with a 30% uncertainty assigned to the extrapolated Λ spectra. An additional 20% uncertainty is assigned to account for the uncertainty in the Σ^+ yields.

At low p_T region, there is another method for $\bar{p}$ feed-down correction independent of the Λ and Σ spectra measurement. The dca distribution of the primordial $\bar{p}$ and the $\bar{p}$ from weak decays are different. To derive the primordial $\bar{p}$ yield, we can use these 2 dca distributions to fit the inclusive $\bar{p}$ dca distribution by the lease χ^2 method.

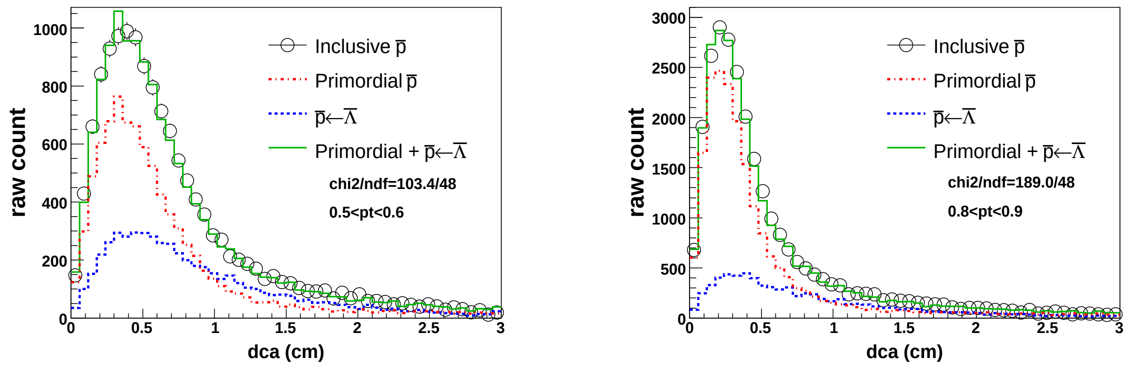

Figure 3.13: Dca fitting method the derive the primordial $\bar{p}$.

Fig. 3.13 shows the dca fitting method in two p_T bins. Blue dashed lines and red dashdotted lines represent the simulated dca distributions for weak decays and primordial $\bar{p}$, respectively. Green solid lines represent the sum of two simulated dca distributions and the black circles represent the inclusive $\bar{p}$ dca distributions for real data.

3.5 Light nuclei identification and efficiency

3.5.1 PID technique for light nuclei

Fig. 3.14 presents the particle identification techniques and methods. Fig. 3.14 (a) shows the ionization energy loss (dE/dx) of charged tracks as a function of rigidity ($rigidity = |momentum/charge|$) measured by the TPC at $-1 < \eta < 1$. Fig. 3.14 (b) shows Z distribution for ^3He and $\overline{^3He}$ signals. Z is defined in Eq. 3.5.

$$Z = log(\frac{dE/dx|_{measure}}{dE/dx|_{predict}}) \tag{3.5}$$

Table 3.2: Track selection for light nuclei

nFitPts	> 24
ndEdxPts	> 14
η	(-1, 1)
global dca (cm)	(0.0, 1.0)

After tight track quality selections, which is listed in Table. 3.2, the $^3He(\overline{^3He})$ signals are essentially background free. We use counting method to derive the yields. For the $d(\overline{d})$ identification, we use the normalized dE/dx parameter $n\sigma_d$. Fig. 3.14 (c) shows $n\sigma_d$ (extracted from dE/dx) distribution for $\overline{d}$ at $0.7 < p_T < 1.0$ GeV/c. The signal is fit with a Gaussian function and an exponential background. Fig. 3.14 (d) shows m^2 distribution for d at $2.5 < p_T < 3.0$ GeV/c measured by TOF after the dE/dx selections. The signal is fit with a Gaussian function and a linear background.

3.5.2 Efficiencies and corrections

Like pion and proton, the tracking efficiency of deuteron is also studied by Monte Carlo simulations, which is shown in Fig. 3.15. We don't have such Monte Carlo simulations for ^3He. Since we only study the ^3He spectra at high p_T ($2 < p_T < 6$ GeV/c), we can take the deuteron high p_T plateau value as the best estimate.

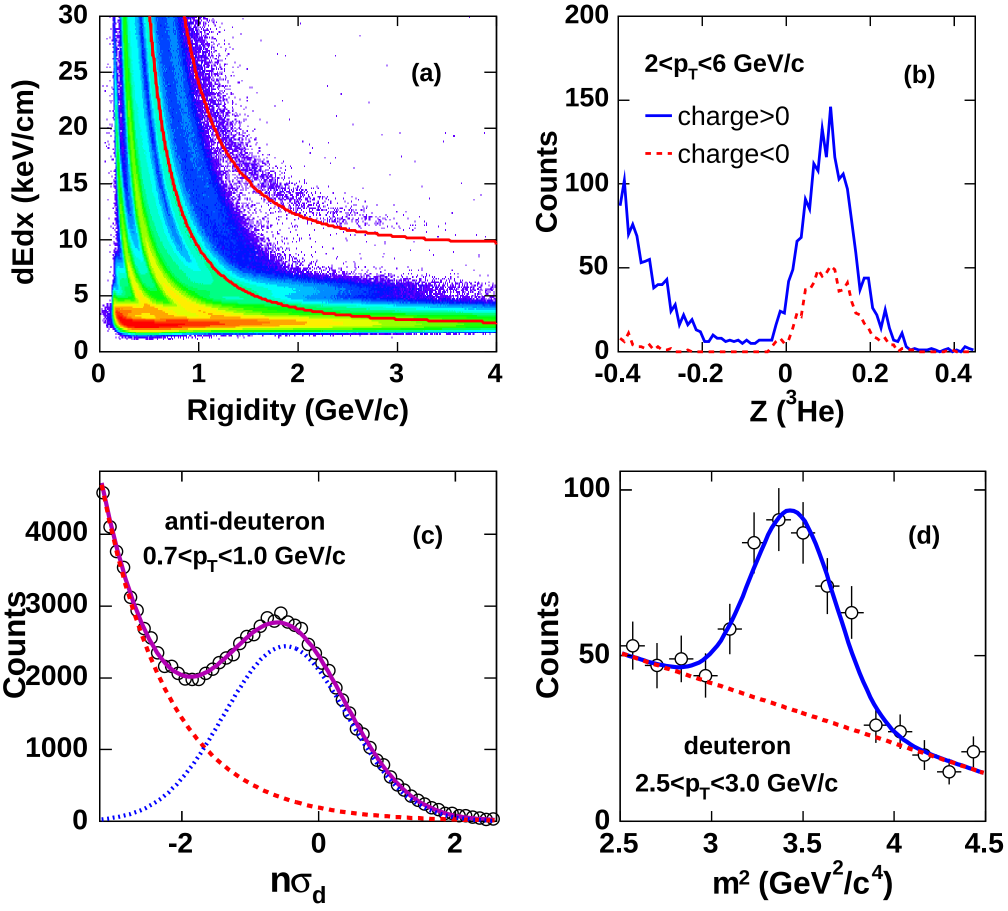

Figure 3.14: (a) TPC dE/dx as a function of rigidity. Lines are expected values for $d(\overline{d})$ and $^3He(\overline{^3He})$ predicted by the Bichsel function. (b) Z distribution of ^3He (solid line) and $\overline{^3He}$ (dashed line). (c) $n\sigma_d$ distribution of $\overline{d}$ at $0.7 < p_T < 1.0$ GeV/c with a Gaussian fit including an exponential background. (d) $m^2(m^2 = (p/\beta/\gamma)^2)$ distribution for d from TOF after TPC dE/dx selections at $2.5 < p_T < 3.0$ GeV/c, with a Gaussian fit including a linear background.

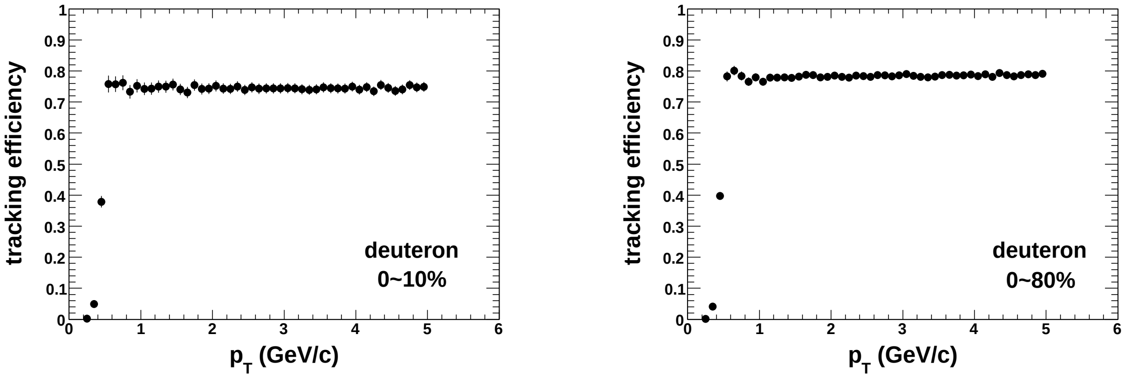

Figure 3.15: Deuteron tracking efficiency as a function of p_T. The left panel is for 0-10% centrality and the right panel is for 0-80% centrality.

The STAR GEANT simulations have no software packages for $\bar{d}$ or $\overline{^3He}$. We have to use Eq. 3.6 to estimate the annihilation effect for anti-nuclei [53].

$$\sigma_{inel}(d,^3He) \approx (\sqrt{2}, 2)\sigma_{inel}(p) \tag{3.6}$$

In Eq. 3.6, $\sigma_{inel}(X)$ is the annihilation cross-section for the anti-X particle and all the particles need to have the same momentum per nucleons. For $\bar{p}$, the annihilation cross-section can be studied by the tracking efficiencies discrepancy between p and $\bar{p}$. Fig. 3.16 shows the $\bar{p}$ annihilation effect as a function of p_T and this effect is insensitive to the centrality.

In the d and $\bar{d}$ spectra analysis, the TOF matching efficiency correction is also required. The matching efficiency is estimated by the same method used in hadron spectra analysis. Fig. 3.17 shows the d and $\bar{d}$ matching efficiency.

3.6 Reaction plane method for v_2 calculation

In heavy ion collisions, the event plane is reconstructed from the detected final particle azimuths. The acceptance and efficiency of the detectors in azimuth is corrected by compensating the azimuth to a flat distribution with Φ weights. Technically, the Φ weights are created for different days to deal with the different situations in a long

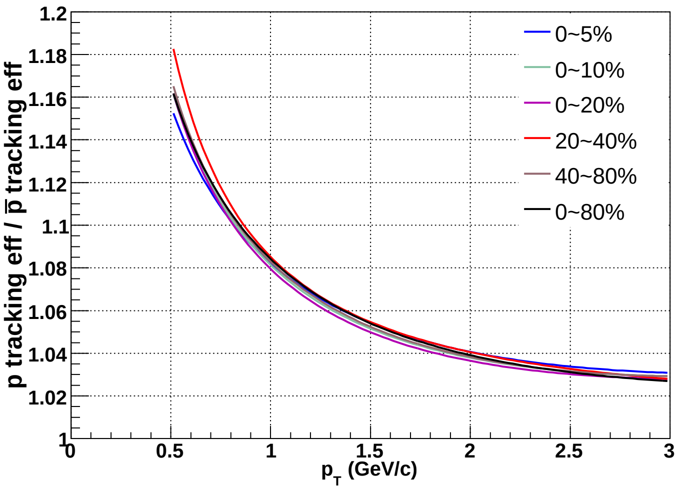

Figure 3.16: p tracking efficiency over $\bar{p}$ tracking efficiency as a function of p_T in different centrality bins.

running period. The second order harmonic event plane azimuth Ψ_2 can be calculated from the $\overrightarrow{Q}$ vector, as Eq. 3.7,3.8:

$$\Psi_2 = \left(\arctan\frac{Q_y}{Q_x}\right)/2, \qquad 0 < \Psi_2 < \pi \tag{3.7}$$

$$\overrightarrow{Q} = (Q_x, Q_y) = \left(\sum_i w_i \cdot \cos(2\phi_i), \quad \sum_i w_i \cdot \sin(2\phi_i)\right) \tag{3.8}$$

Here, w_i is the weight for each track included in the event plane calculation, which includes both the Φ weight and the p_T weight. Fig. 3.18 shows a Φ weight distributions for a single day. The tracks selected in the event plane calculation should satisfy the criteria listed in Table. 3.3.

Fig. 3.18 shows a typical Φ weight distribution. Fig. 3.19 shows the event plane angle distribution before and after the Φ weight correction. It is clear that the Φ weight correction is necessary.

The resolution of the event plane is calculated using the sub-event method [54]. Each event is divided into two sub-events with nearly equal multiplicity by 3 different

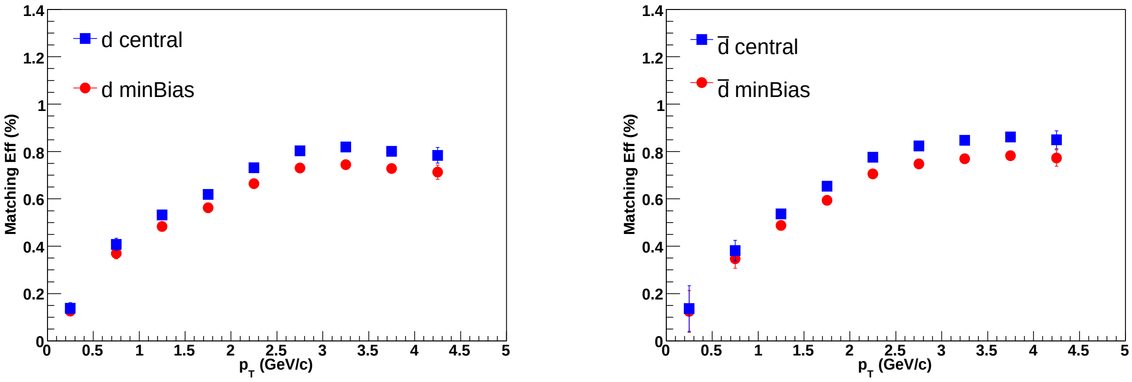

Figure 3.17: d (left panel) and $\bar{d}$ (right panel) matching efficiency as a function of p_T for central and minBias triggered events.

Table 3.3: Track selection in event plane calculation

nFitPts	≥ 15
nFitPts/nMax	> 0.52
p_T (GeV/c)	(0.1, 2.0)
η	(-1, 1)
global dca (cm)	(0.0, 2.0)

ways, random, the charge of tracks and the η of tracks . The event plane is reconstructed in each sub-event, denoted as Ψ_2^a and Ψ_2^b. Then the event plane resolution $r = \langle cos[2(\Psi_2 - \Psi_{rp})]\rangle$ can be calculated from Eq.(14) and (11) from [54]:

$$\langle\cos[2(\Psi_2 - \Psi_{rp})]\rangle = \frac{\sqrt{\pi}}{2\sqrt{2}}\chi_2 \exp(-\chi_2^2/4) \times [I_0(\chi_2^2/4) + I_1(\chi_2^2/4)] \tag{3.9}$$

$$\langle\cos[2(\Psi_2^a - \Psi_{rp})]\rangle = \sqrt{\langle\cos[2(\Psi_2^a - \Psi_2^b)]\rangle} \tag{3.10}$$

$$\chi_2 = v_2/\sigma = v_2\sqrt{2N} \tag{3.11}$$

Firstly, we obtained the sub-event resolution $\langle\cos[2(\Psi_2^a - \Psi_{rp})]\rangle$ from Eq. 3.10. Then Eq. 3.9 can be solved as an iterative routine to extract the sub-event χ_2^a. This variable is proportional to $\sqrt{N}$ according to Eq. 3.11, so the total event χ_2 is obtained by $\chi_2 = \sqrt{2}\chi_2^a$. After putting this χ_2 into Eq. 3.9, we calculated the final full event resolution. The physical v_2 is calculated as $v_2 = v_2^{obs}/r$, where v_2^{obs} is the observed v_2

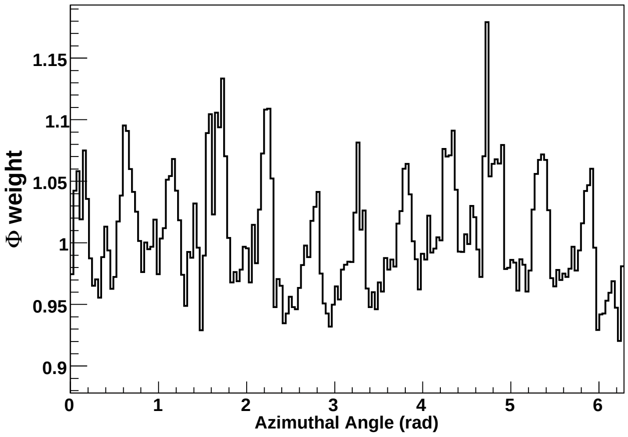

Figure 3.18: a typical Φ weight distribution

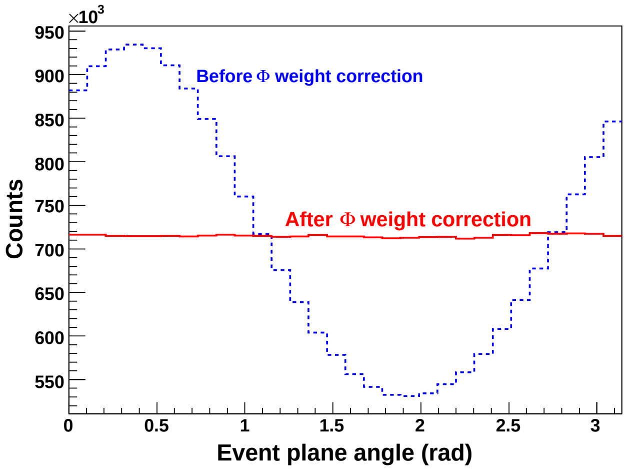

Figure 3.19: Event plane angle distribution before and after the Φ weight correction.

and r is the event plane resolution. The final event plane resolution used for correction is 76% for minbias triggered events and 68% for central triggered events.

Chapter 4

Results on pion and proton spectra

4.1 Pion and proton spectra

The invariant yields $d^2N/(2\pi p_T dp_T dy)$ of $\pi^{\pm}$, p and $\bar{p}$ from Au+Au collisions are shown in Fig. 4.1. Red and black symbols represent the TOF results and the $rdEdx$ results, respectively. The lines in the figure show the proton spectra after feed-down correction. Systematic errors for the TOF measurements are around 8%, which is dominated by the TOF matching efficiency. Systematic errors for the TPC measurements are p_T dependent and include uncertainties in efficiency ($\sim$ 7%), dE/dx position and width (10-20%), K_S^0 constraint (5%), background from decay feed-down and ghost tracks (8-14%), momentum distortion due to charge build-up in the TPC volume (0-10%), the distortion of the measured spectra due to momentum resolution (0-5%) and half of the difference between the two methods (3-Gaussian fitting and directly counting) to extract the proton yields (3-6%). The systematic errors are added in quadrature. The spectra from the TOF and TPC measurements agree within systematic errors in the overlapping p_T region.

4.2 Particle ratios

The Nuclear modification factor (R_cp) for pion (π^++π^-) and proton (p+$\bar{p}$) is shown in Fig. 4.2. In 0-12% central Au+Au collisions, the pion yield shows strong suppression

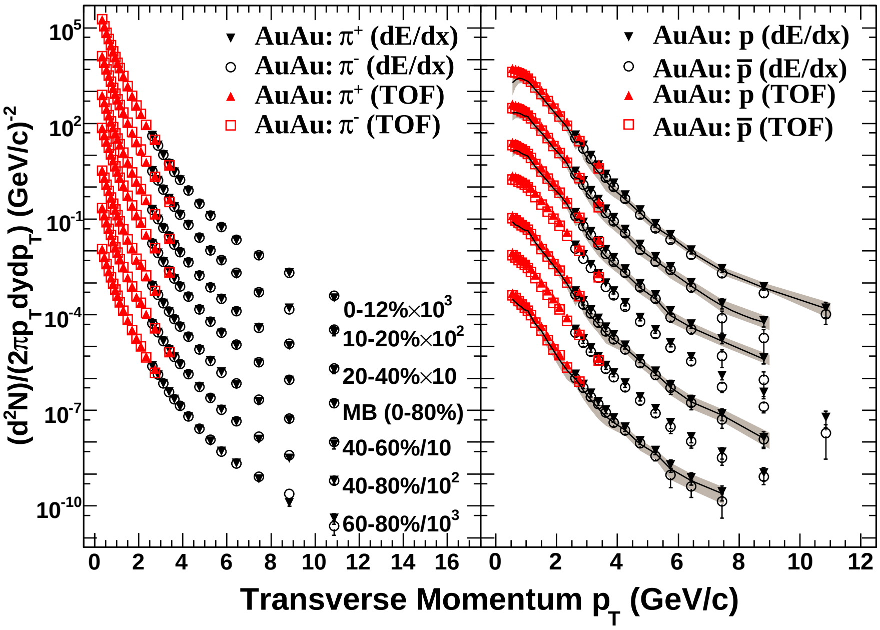

Figure 4.1: Centrality dependence of mid-rapidity ($|y| < 0.5$) $\pi^{\pm}$, p and $\bar{p}$ invariant yields versus p_T from 200 GeV Au+Au collisions. The error bars are the quadrature sum of statistical and systematic errors. The solid lines depict our best estimates of the proton yields corrected for the hyperon (Λ and Σ^+) feed-down. The shaded bands on the lines represent the uncertainties. The order of the spectra in different centralities is the same for both panels.

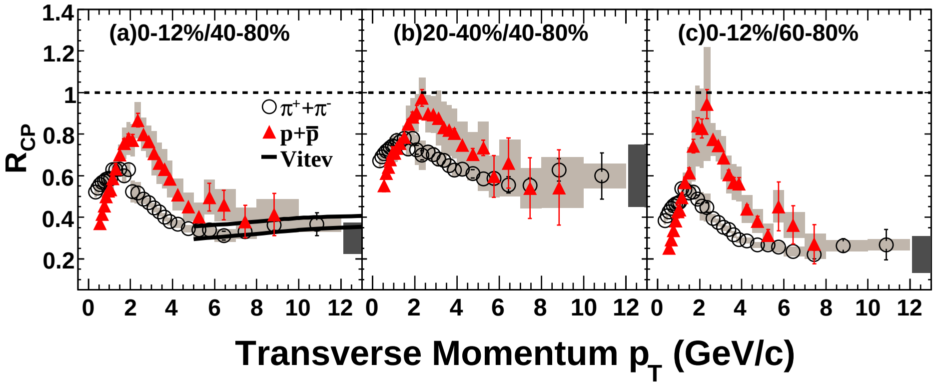

Figure 4.2: Nuclear modification factors R_{CP} for $\pi^{+}+\pi^{-}$ and $p+\bar{p}$ in 200 GeV Au+Au collisions. The point-to-point systematic uncertainties are shown as the shaded boxes around the data points. The dark shaded bands show the normalization systematic uncertainty in the number of binary collisions. The solid lines show jet quenching predictions for pions [55].

with R_{CP} between 0.2 and 0.4 at $p_T \geq 3\ GeV/c$. This is consistent with the jet quenching calculation [55] shown in Fig. 4.2 (a). For each centrality, the R_{CP} values for protons peak at $p_T \sim$ 2-3 GeV/c. At intermediate p_T, p and $\bar{p}$ are less suppressed, with respect to binary scaling, than $\pi^{\pm}$, but a significant suppression is still observed in central Au+Au collisions. This is in contrast to nuclear modification factors in d+Au collisions, where a significant enhancement is seen for protons [56]. Previous measurements at lower transverse momentum [61] showed that R_{CP} for protons is close to 1 for $1.5 < p_T < 4.5$ GeV/c. Our results agree with those measurements within systematic errors, but our data do not suggest that R_{CP} is constant over the range $1.5 < p_T < 4.5$ GeV/c and the extended p_T reach shows that R_{CP} for protons decreases again at higher p_T.

The results in Fig. 4.2 clearly show different R_{CP} for protons and pions at intermediate p_T. A similar effect has been observed for K^0_S and Λ [13], with K^0_S (Λ) R_{CP} similar to pion (proton) R_{CP}. The grouping of particle production according to the number of constituent quarks has been attributed to quark coalescence at

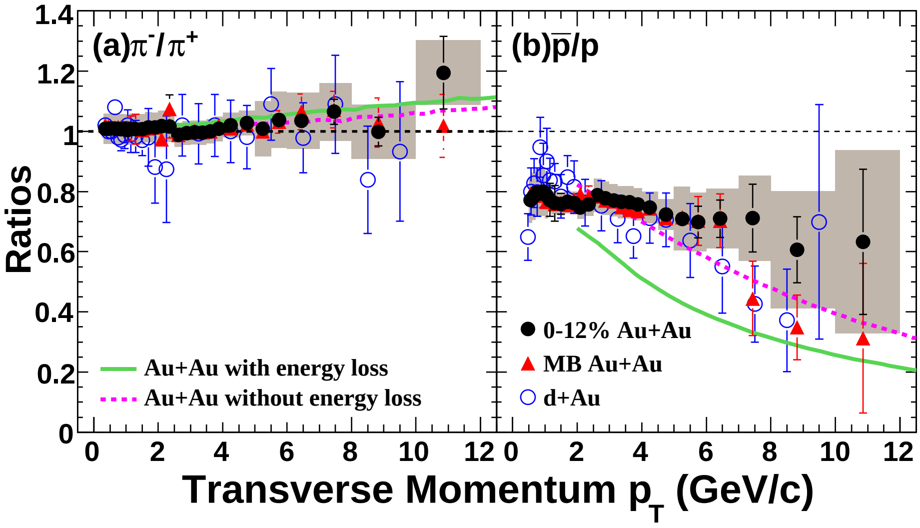

Figure 4.3: The π^-/π^+ and $\bar{p}/p$ ratios in 12% central, MB Au+Au and d+Au [45, 56] collisions at $\sqrt{s_{NN}} = 200$ GeV. The shaded boxes represent the systematic uncertainties in the top 12% central Au+Au collisions. The systematic uncertainties for MB Au+Au collisions are similar. Curves are the corresponding predictions from a jet quenching model [57].

hadronization from a collective partonic medium [62, 59, 60, 63]. Our high statistics measurements show that these effects disappear at high p_T, where baryons and mesons show a common degree of suppression. This is consistent with the general expectation that collective and coalescence effects have a finite p_T reach.

Fig. 4.3 shows the π^-/π^+ and $\bar{p}/p$ ratios in 0-12%, MB Au+Au, and d+Au [45, 56] collisions. We observe that the π^-/π^+ ratios are consistent with unity in d+Au, MB and central Au+Au collisions. Predictions from a pQCD based model with and without partonic energy loss are consistent with our data [57]. The same calculation shows a significant effect from energy loss on the $\bar{p}/p$ ratio (Fig. 4.3 (b)), due to the large energy loss of gluons in the medium. Our measurements, in contrast, show little centrality dependence of the $\bar{p}/p$ ratio at $p_T \leq 6\ GeV/c$ and a possible increase of the $\bar{p}/p$ ratio at higher p_T in central Au+Au collisions compared to d+Au collisions.

Fig. 4.4 shows the p/π^+ and $\bar{p}/\pi^-$ ratios in 0-12%, 60-80% Au+Au and d+Au [45,

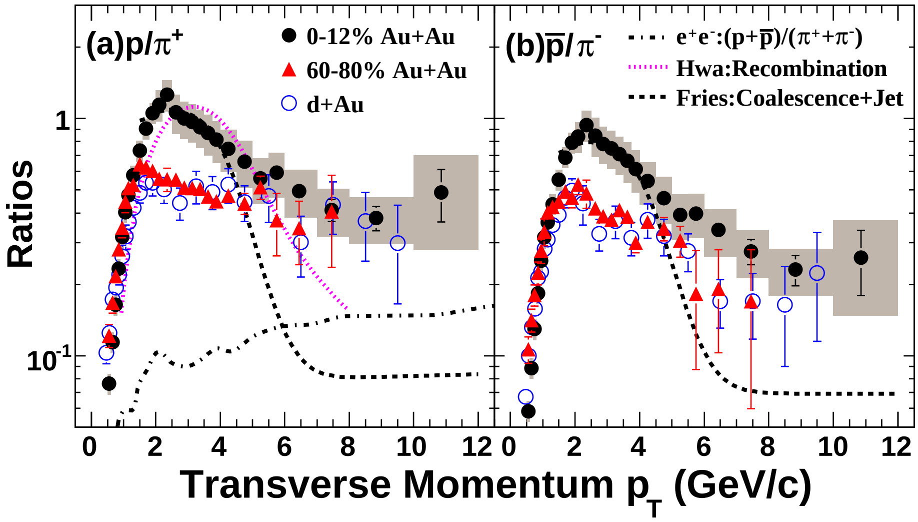

Figure 4.4: The p/π^+ and $\bar{p}/\pi^-$ ratios from d+Au [45, 56] and Au+Au collisions at $\sqrt{s_{NN}} = 200$ GeV. The $(p + \bar{p})/(\pi^+ + \pi^-)$ ratio from light quark jets in $e^+ + e^-$ collisions at $\sqrt{s} = 91.2$ GeV are shown as a dotted-dashed line [58]. The shaded boxes represent the systematic uncertainties in the top 12% central Au+Au collisions. The systematic uncertainties for 60-80% Au+Au collisions are similar. The dotted and dashed lines are model calculations in central Au+Au collisions [59, 60].

56] collisions. The ratios in Au+Au collisions are observed to be strongly centrality dependent at intermediate p_T. In central Au+Au collisions, the p/π^+ and $\bar{p}/\pi^-$ ratios peak at $p_T \sim 2 - 3\ GeV/c$ with values close to unity, decrease with increasing p_T, and approach the ratios in d+Au, p+p and peripheral Au+Au collisions at $p_T \geq 5\ GeV/c$. The dotted and dashed lines are predictions for central Au+Au collisions from recombination [59] and coalescence with jet quenching and KKP fragmentation functions [60, 64], respectively. These models can qualitatively describe the $p(\bar{p})/\pi$ ratio at intermediate p_T but in general under-predict the results at high p_T.

At high p_T, the p/π^+ ratios can be directly compared to results from quark jet fragmentation as measured in $e^+ + e^-$ collisions by DELPHI [58], indicated by the dotted-dashed line in Fig. 4.4 (a). The p/π^+ ratio measurements in d+Au and Au+Au collisions are higher than in quark jet fragmentation. This is likely due to a significant contribution from gluon jets to the proton production, which have a $(p+\bar{p})/(\pi^+ + \pi^-)$ ratio up to two times larger than quark jets [15]. A similar comparison cannot be made for $\bar{p}$ production (Fig. 4.4 (b)), because there is a significant imbalance between quark (q) and anti-quark ($\bar{q}$) production at high p_T in d+Au and Au+Au collisions and the fragmentation function of q to $\bar{p}$ can not be readily derived from $e^+ + e^-$ collisions. It is, however, known from lower beam energies, where quark fragmentation is dominant, that the $\bar{p}/\pi$ and $\bar{p}/p$ ratios from quark jets are very small ($<\sim 0.1$) [56, 65]. The large $\bar{p}/\pi^-$ ratio of ≈ 0.2 seen in Fig. 4.4 (b) is likely dominated by gluon fragmentation. This is in agreement with AKK fragmentation functions [66] which describe the STAR data in p+p collisions [56], showing that gluon fragmentation contributes to 40% of pion production at $p_T \simeq 10\ GeV/c$ while more than 80% of $p + \bar{p}$ are from gluon fragmentation.

At high p_T, the nuclear modification factor of protons is similar to that of pions (Fig. 4.2) and the p/π^+, $\bar{p}/\pi^-$, and $\bar{p}/p$ ratios in central Au+Au collisions are similar to those in p+p and d+Au collisions [56]. These observations indicate that at sufficiently high p_T, fragmentation in central Au+Au and p+p events is similar and that there is no evidence of different energy loss for quarks and gluons in the medium. The theoretical calculations in Fig. 4.3 show that differences in radiative energy loss are expected to result in measurable changes in the $\bar{p}/p$ and $\bar{p}/\pi^-$ ratios. Those calculations, however, do not reproduce the measured p and $\bar{p}$ spectra in p+p collisions [56], indicating that the fragmentation functions for baryon production are not well known. The determination of baryon fragmentation functions from elementary collisions and the expected range of validity of factorization for baryon production are areas of ongoing investigation [56, 66]. In addition, there is some uncertainty in the mechanism of energy loss. It has been postulated that the addition of collisional energy loss to radiative energy loss may explain the large suppression of leptons from heavy flavor decays in Au+Au collisions [67, 68]. The latest calculations [69, 23] including collisional energy loss and path length fluctuations [70] show that the nuclear modification factor of gluons is still expected to be a factor of three lower than that of light quarks.

Chapter 5

Results on nuclei production

5.1 Spectra

The invariant yields $d^2N/(2\pi p_T dp_T dy)$ of $d(\overline{d})$ and ${}^3He(\overline{{}^3He})$ from Au+Au collisions are shown in Fig. 5.1. Systematic errors of d and $\bar{d}$ are estimated 20%-25% totally, including the uncertainty of TOF matching efficiency 15%-20%, TPC tracking efficiency 10% and the fitting method 5%-15%. Systematic errors of ${}^3He$ and $\overline{{}^3He}$ are estimated to be 10%, which is dominated by the TPC tracking efficiency.

5.2 Coalescence parameters

Fig. 5.2 shows the extracted coalescence parameters B_2 and B_3 for $d(\overline{d})$ and ${}^3He(\overline{{}^3He})$. B_2 for $d(\overline{d})$ is consistent with $\sqrt{B_3}$ for ${}^3He(\overline{{}^3He})$, which indicates that the correlation volumes for $d(\overline{d})$ and ${}^3He(\overline{{}^3He})$ are similar. Both B_2 and B_3 show strong centrality dependence. In more central collisions, a smaller coalescence parameter indicates that the correlation volume at thermal freeze-out is larger and the probability of formation of light nuclei is less.

Figure 5.3 shows the comparisons between the coalescence parameters and the pion interferometry (HBT) results. For the calculation of the freeze-out volume we

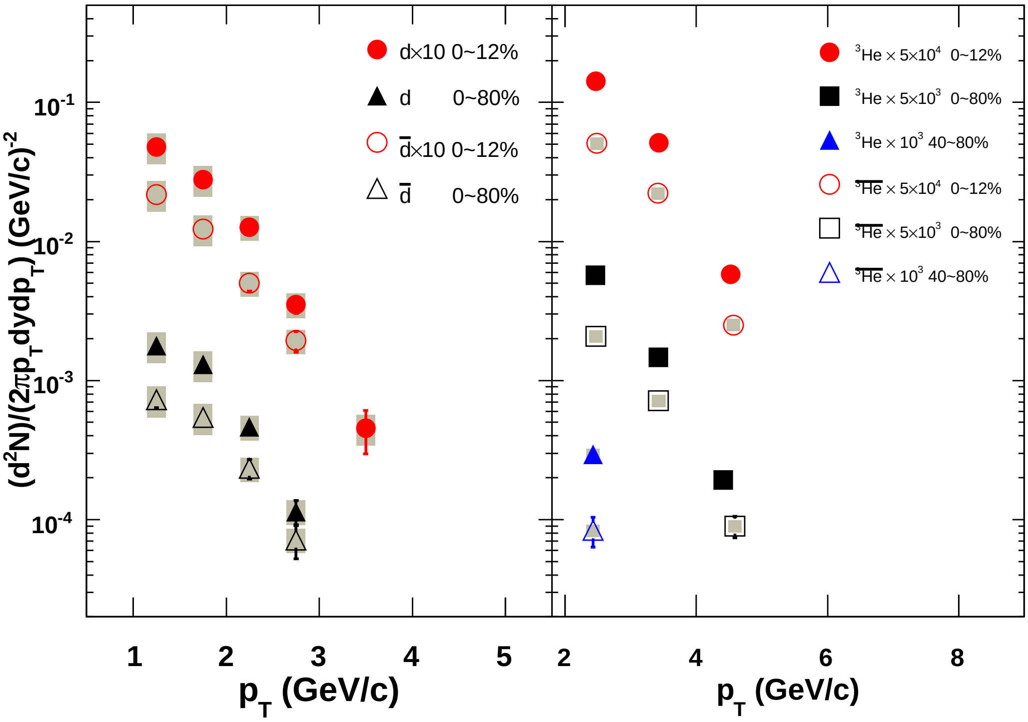

Figure 5.1: p_T spectra of $d(\overline{d})$ (left panel) and $^3He(\overline{^3He})$ (right panel) for different centralities. Solid symbols and open symbols represent the positive charged particles and negative charged particles respectively. The shaded bands represent the systematic uncertainties.

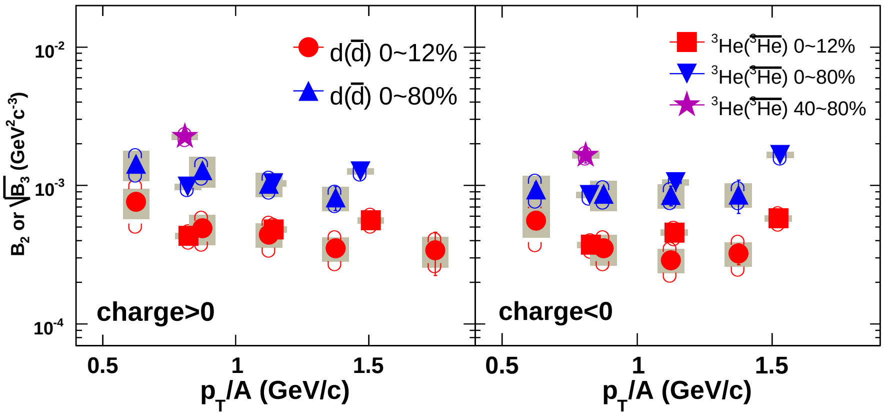

Figure 5.2: Coalescence parameters B_2 and $\sqrt{B_3}$ as a function of p_T/A for positive charged particles (left panel) and negative charged particles (right panel). The lines and bands show statistical and systematic errors due to the light nuclei spectra measurement, respectively. The brackets show the uncertainties of the FD correction for the proton and anti-proton.

use the following expression:

$$V_f = (2\pi)^{3/2} \cdot R_{long} \cdot R_{side}^2 \tag{5.1}$$

Where V_f is the freeze-out volume. R_{long} and R_{side} are the longitudinal and sideward radii, respectively. A density distribution of Gaussian shape in all three dimensions is assumed. R_{long} and R_{side} values are taken from Ref. [71] ($k_T = 0.2\ GeV/c$). In Figure 5.3 the $d(\overline{d})$ and $^3He(\overline{^3He})$ transverse momentum ranges are $1.5 < p_T < 2.0\ GeV/c$ and $2.0 < p_T < 2.5\ GeV/c$, respectively. B_2 and $\sqrt{B_3}$ are proportional to $1/V_f$ in different centrality collisions, which indicates that the freeze-out volume of nucleus is proportional to that of pions.

5.3 Elliptic flow parameter v_2

Fig. 5.4 (a) shows v_2 as a function of p_T for $d+\overline{d}$, $^3He+\overline{^3He}$ and $\overline{d}$ in minimum-bias collisions. When both v_2 and p_T are scaled by A, the results are shown in Fig. 5.4 (b). The baryon v_2 [72] is also shown as the solid line. $d+\overline{d}$ and baryon v_2 follow

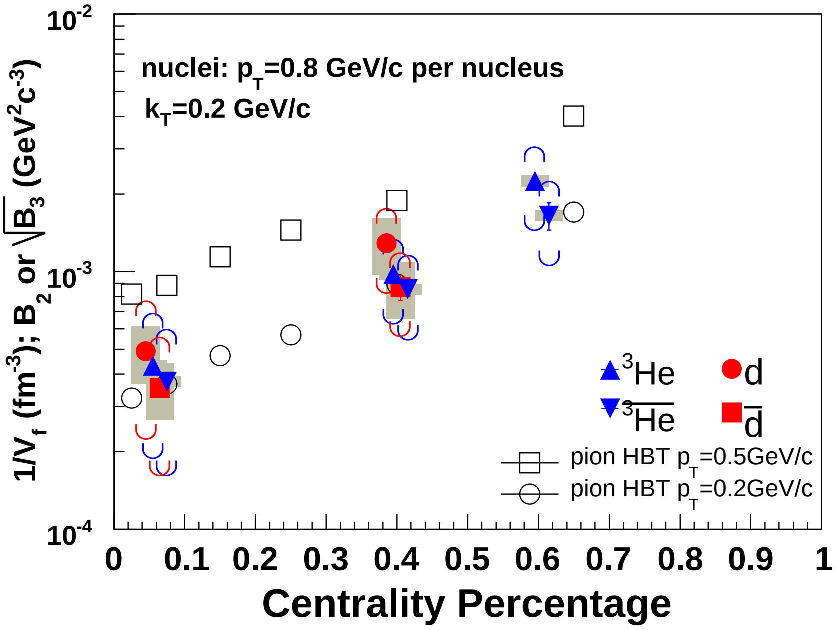

Figure 5.3: Coalescence parameters (filled symbols) B_2 and $\sqrt{B_3}$ as a function of centrality fraction for $d(\overline{d})$ and $^3He(\overline{^3He})$. The STAR HBT measurements (open symbols) are also shown. See details in the text. For the nuclei results, the lines and bands show statistical and systematic errors due to the light nuclei spectra measurement, respectively. The brackets show the uncertainties of the FD correction for the proton and anti-proton.

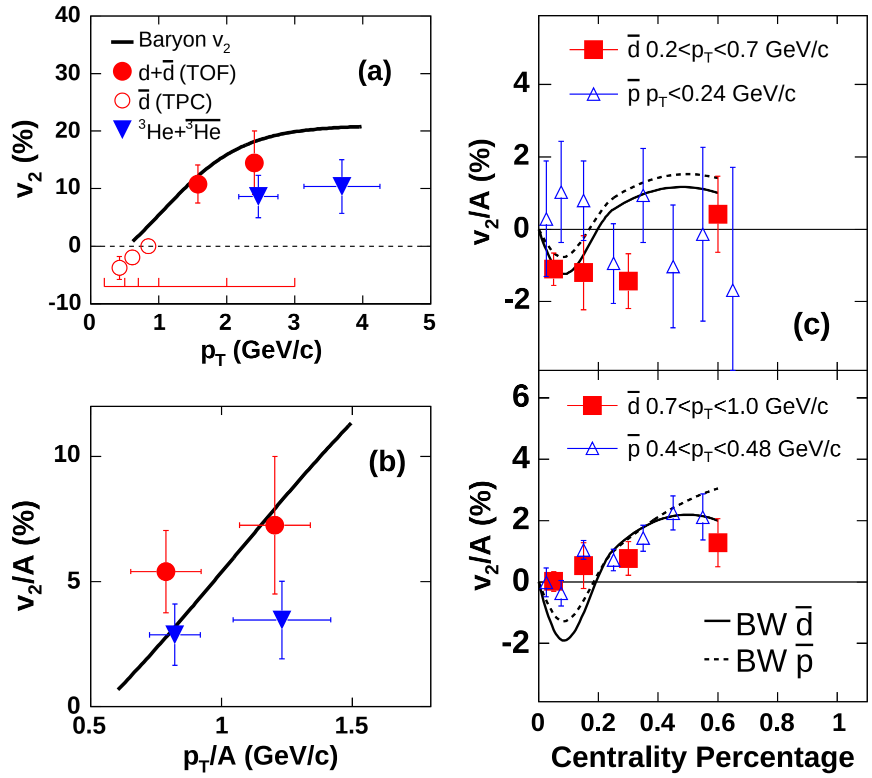

Figure 5.4: (a) The elliptic flow parameter v_2 from minimum bias collisions as a function of p_T for ${}^3He + \overline{{}^3He}$ (triangles), $d + \overline{d}$ (filled circles) and $\overline{d}$ (open circles); solid line represents the baryon v_2. (b) $d+\overline{d}$ and ${}^3He+\overline{{}^3He}$ v_2 as a function of p_T, both v_2 and p_T have been scaled by A. Errors are statistical only. (c) Low p_T $\overline{d}$ v_2/A (filled squared) as a function of centrality fraction ($0-10\%$, $10-20\%$, $20-40\%$, $40-80\%$, respectively). Errors are statistical only. $\overline{p}$ v_2 is also shown as open triangles. Blast-wave predictions are show as solids lines ($\overline{d}$) and dashed lines ($\overline{p}$).

the A scaling within errors. It indicates that the $d + \overline{d}$ are formed through the coalescence of $p(\overline{p})$ and $n(\overline{n})$ just before the thermal freeze-out. It seems that the scaled $^3He + \overline{^3He}$ v_2 deviates from the the baryon v_2. Poor statistics limit drawing further conclusions. The $\overline{d}$ v_2/A as a function of centrality percentage is shown in Fig. 5.4 (c). The two panels represent results for two different regions of p_T. In the p_T region $0.2 < p_T < 0.7$ GeV/c, $\overline{d}$ has a negative v_2 in central and mid-central collisions. This negative v_2 is consistent with a large radial flow, as the blast-wave predictions show. At the same p_T/A where the $\overline{d}$ v_2 is negative, the $\overline{p}$ v_2 is consistent both with zero and with the $\overline{d}$ v_2, due to large uncertainties. Though the blast-wave model predicts the generic feature of negative v_2, quantitative agreement between data and model throughout the entire centrality and p_T range is lacking.

Chapter 6

Anti-baryon phase space density and source of anti-baryon production

6.1 Anti-baryon phase space density

The coalescence measurement is sensitive to the phase space of baryon and anti-baryon [18, 73]. $\bar{d}/\bar{p}$ (ratio of the differential cross section) can be taken as a measure of the anti-baryon phase space density at kinetic freeze-out where coalescence happens. See Chapter 1 for details.

Data of $\bar{d}/\bar{p}$ ratio from various beam energies and colliding species ($pp, \bar{p}p, pA, AA$) [10, 74, 75, 76, 77, 78, 79, 80, 81, 82, 83] were collected and shown in Fig. 6.1. One very interesting observation is that the ratio increases monotonically with beam energies and reaches a plateau above ISR beam energy regardless of the beam species (pp, pA, AA). Similar behavior has been seen in $\bar{p}/p$ ratio as a function of beam energy [84].

The relation between $\bar{d}/\bar{p}$ and $\bar{p}/p$ is

$$\bar{d}/\bar{p} \simeq \exp\left(-m_B/T\right) \times \sqrt{\bar{p}/p}$$

where m_B is the nucleon mass and T is the freeze-out temperature. The curves in Fig. 6.1 correspond to three choices of $T = 130, 120, 110\ MeV$. This relation

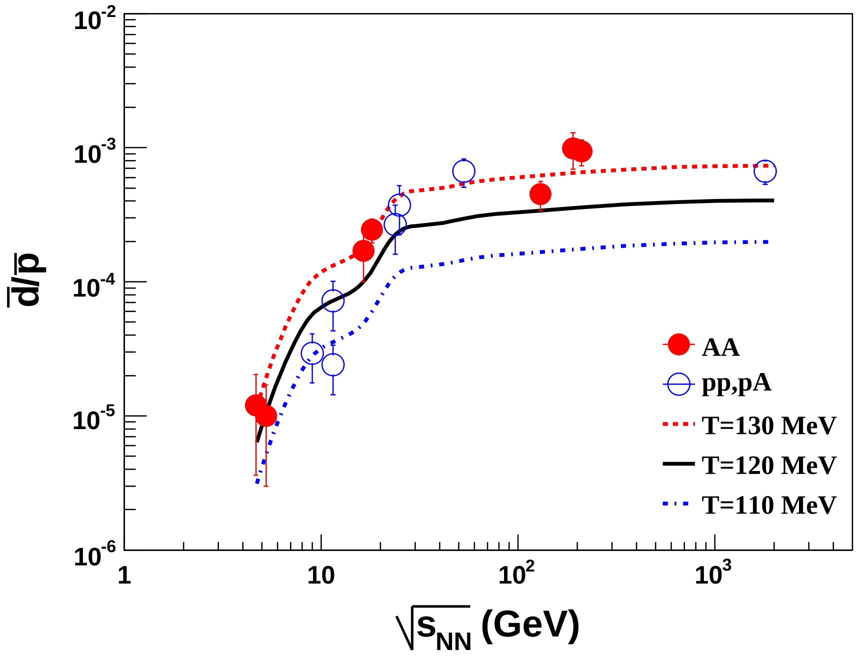

Figure 6.1: $\bar{d}/\bar{p}$ as a measure of antibaryon phase space density as a function of beam energy for pp, pA and AA collisions. The curves are $\exp\left(-m_B/T\right) \times \sqrt{\bar{p}/p}$ for three choices of T at 130 MeV, 120 MeV and 110 MeV.

shows qualitative agreement with a fixed freeze-out temperature at about 120 MeV. Recently, CERES Collaboration observed a universal thermal freeze-out behavior [21]. These two measurements may be closely related. However, It also indicates that the temperature may slightly depend on beam energy with lower temperature at lower $\sqrt{s}$ and higher value at higher $\sqrt{s}$. These findings suggest that the anti-nucleons are produced and coalesce in a statistical fashion in $A+A$, $p+A$, $p+p$ and γp collisions at similar density. Final state interactions in nucleus-nucleus collisions do not change this aspect. It also shows that correlations among anti-nucleons in momentum and coordinate space do not alter the $\bar{d}$ yields since its production can be described statistically.

6.2 The source of anti-deuterons production

system	processes	$\bar{d}/\bar{p}$
$e^+e^-(\Upsilon)$	ggg	$7.4^{+3.6}_{-2.0}10^{-4}$
$\gamma p(200)$	$q\bar{q}g$	$5.0 \pm 1.1 \times 10^{-4}$
$pp(53)$	$qg, \bar{q}g$	$5.0 \pm 1.2 \times 10^{-4}$
$p\bar{p}(1800)$	$qg, \bar{q}g$	5.0×10^{-4}
$AA(130)$	$qg, \bar{q}g$	$4.5 \pm 1.1 \times 10^{-4}$
$e^+e^-(10)$	$q\bar{q}$	$< 2.1 \times 10^{-4}$
$e^+e^-(91)$	$q\bar{q}$	$(8.4 \pm 2.7) \times 10^{-5}$
$pp(A)(< 20)$	qg, qq	$< 10^{-4}$
$AA(< 20)$	qg, qq	$10^{-4} - 10^{-5}$

Table 6.1: Dominant processes in different collision systems and the corresponding $\bar{d}/\bar{p}$ ratio. Values in the parentheses are the center of mass beam energy in GeV.

We tabulate the collision system, their dominant processes and $\bar{d}/\bar{p}$ in Tab. 6.1. Table 6.1 and Fig. 6.2 show that collisions dominated by $\bar{q}+g$ and/or $g+g$ saturate anti-baryon density at 10^{-3} while those dominated by $q+q(\bar{q})$ or $q+g$ produce much less anti-baryons [85, 86, 87]. It is very convincing from the collisions in γp and e^+e^- at various energies. The measurements at e^+e^- and γp may be used to gauge what kind of partonic configuration creates baryons. There are two measurements of $\bar{d}/\bar{p}$ from e^+e^- at low energies [85]: one at Υ mass of $\sqrt{s} = 9.86$ where the final state hadrons are predominantly from Υ decay to three gluons (ggg) and the other an upper limit at continuous energy of $\sqrt{s} = 10.GeV$ where the final state hadrons come from $q\bar{q}$ pair from a virtual photon. These two ratios are different by more than a factor of 3. This may be related to how baryons are created (more baryon from gluons than from quarks). In fact, not only the $\bar{d}/\bar{p}$ are different in these two e^+e^- collisions, the baryon production is higher at Υ than at the continuous energy while the meson production is the same. The anti-baryon phase space density from ggg configuration in e^+e^- is very similar to the anti-baryon phase space density measured at RHIC. The $\bar{d}/\bar{p}$ ratio from the $\bar{q}q$ configuration is much lower. On the other hand, γp collisions [86], where the dominant process is $q\bar{q} + g$, yield similar anti-baryon density as those in nucleus-nucleus collisions.

In addition, ALEPH Collaboration [87] found that baryon production is suppressed in e^+e^- to hadron event relative to other system as shown in Fig. 6.2. The double ratio of $\bar{d}/\bar{p}$ in e^+e^- between Z boson hadron decay events ($\bar{d}/\bar{p} = 8.4 \pm 2.7 \times 10^{-5}$) and $\Upsilon \rightarrow ggg$ events ($\bar{d}/\bar{p} = 7.4^{+3.6}_{-2.0} \times 10^{-4}$) is $\gamma_B = 0.11^{+0.05}_{-0.06}$. In those Z boson hadron events, the dominant process is $q\bar{q}$ fragmentation. However, the event rate of process $q\bar{q}g$, whose fragmentation would yield same $\bar{d}/\bar{p}$ as in ggg, is suppressed by a factor of strong coupling constant $\alpha_s(M_Z) = 0.116$. We have shown in Table 6.1 and Fig. 6.2 that production of anti-deuterons is negligible in $q\bar{q}$ compared to $q\bar{q}g$ events, and both ggg (Υ) and $q\bar{q}g$ (γp) saturate $\bar{d}/\bar{p}$. The suppression of $\bar{d}/\bar{p}$ by a factor of $\gamma_B = 0.11$ in e^+e^- at LEP can be readily explained by the event rate $e^+e^- \rightarrow q\bar{q}g$ at $\alpha_s(M_Z) = 0.116$. This observation can be further tested by measuring $\bar{d}/\bar{p}$ in $e^+e^- \rightarrow \bar{q}q$ and $e^+e^- \rightarrow \bar{q}qg$ separately at LEP or other facilities. The baryon production in a gluon jet is indeed about a factor of 2 higher than that in a quark jet as measured separately at LEP. This will not explain a factor of 10 differences in baryon phase space density. On the other hand, the particle spectra in a gluon jet are in general softer than those in a quark jet. This condensation in momentum and coordinate spaces increases the phase space density of the baryons. From Table 6.1, it is inconclusive whether $q + g$ produces less anti-baryons at low beam energy due to low production of anti-deuteron in this configuration or due to energy threshold

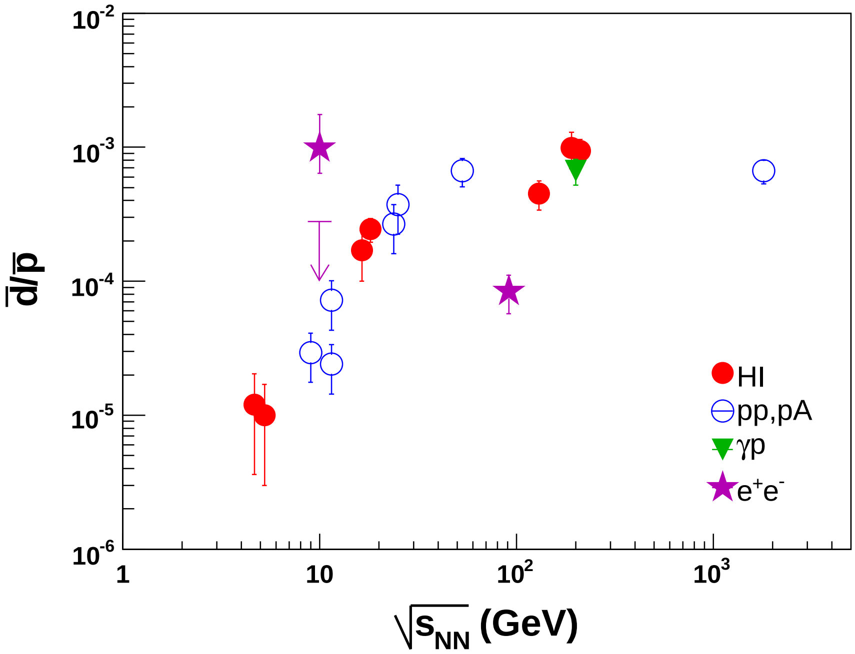

Figure 6.2: $\bar{d}/\bar{p}$ as a measure of antibaryon phase space density as a function of beam energy for various beam species. e^+e^- and γp collisions are also shown at their center of mass beam energy.

in producing anti-deuterons. In any case, it is conclusive that baryon density from collisions involving a gluon is much higher than those without gluon.

Chapter 7

Conclusion and discussion

7.1 Results summary

In this thesis, we have used the particle identification capability of the STAR TPC and TOF detectors to measure the $\pi^{\pm}$ and $p(\bar{p})$ spectra in large transverse momentum range ($0.3 < p_T < 12\ GeV/c$). Benefitting from the high statistic data sample taken in RHIC Run IV, we have measured the ${}^3He(\overline{{}^3He})$ p_T spectra and v_2 at intermediate p_T region ($2 < p_T < 6\ GeV/c$) and $d(\bar{d})$ p_T spectra and v_2 at $1 < p_T < 4\ GeV/c$. The coalescence parameters B_2 and B_3 are extracted. The low p_T ($0.2 < p_T < 1\ GeV/c$) $\bar{d}$ v_2 has also been measured. We have systematically studied the anti-baryon phase space density inferred from $\bar{d}/\bar{p}$ measurements in various collision systems at various energies. It is found that the anti-baryon density at the final-state coalescence saturates when the process from different collisions involving gluons. Among these measurements, high p_T identified particle (both meson and baryon) spectra, ${}^3He(\overline{{}^3He})$ v_2 and low p_T $\bar{d}$ v_2 are the first achievements in the relativistic heavy-ion collisions.

7.2 Conclusion and discussion

From the p/π^+ and $\bar{p}/\pi^-$ plot (Fig. 4.4) we can see the baryon production is enhanced at intermediate p_T region in central collisions. The same behavior (called relative baryon enhancement) can also be seen in the Λ/K_s^0 ratio [88], which is shown in

Fig. 7.1.

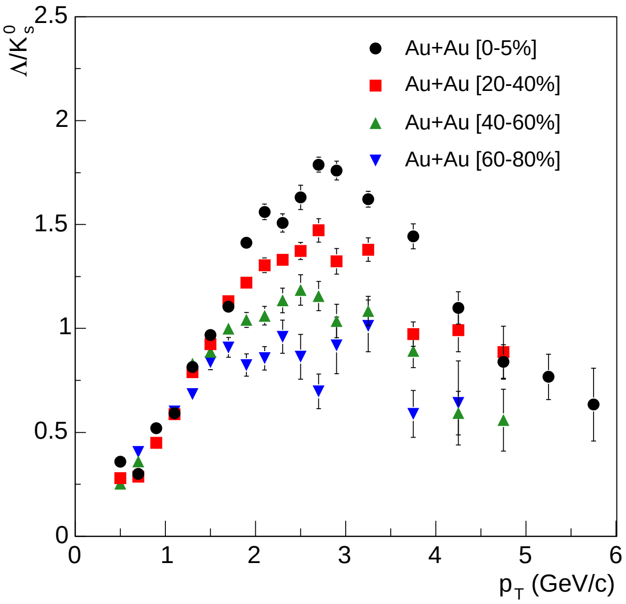

Figure 7.1: The Λ/K_S^0 ratio as a function of centrality and p_T for Au+Au collisions at $\sqrt{s_{NN}} = 200 GeV$.

At the same p_T region, the hadrons elliptic flow is found to follow the number of constituent quark scaling (Fig. 1.5). Coalescence of quarks at hadronization can quantitatively explain these phenomena [13, 14].

We can also study the coalescence processes by measuring the light nuclei. Unlike the partonic coalescence, when the coalescence happens between the nucleons, we can measure both the nuclei and their constituent nucleons and make the comparison between them.

In Chapter 5, the results of coalescence parameters and nuclei v_2 are shown and discussed. As expected, since $B_A \propto (1/V)^{A-1}$, we have found that B_2 and B_3 have smaller values in more central collisions, which indicated that the thermal freeze-out volume is larger in more central collisions. We also found that B_2 has the similar value with $\sqrt{B_3}$ (Fig. 5.2), which means $d(\bar{d})$ and $^3He(\overline{^3He})$ have the similar freeze-out time.

We have compared the B_2 and $\sqrt{B_3}$ to the pion freeze-out volume measured by

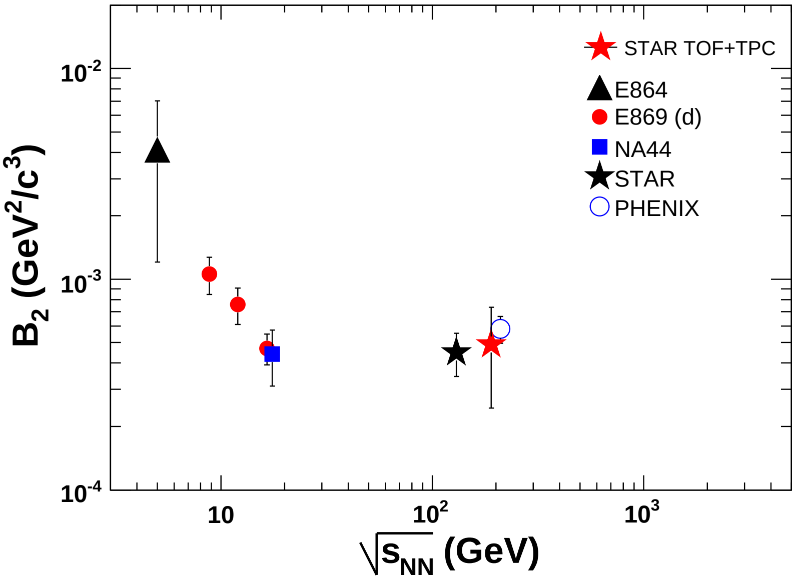

Figure 7.2: Comparison of the coalescence parameter B_2 for d and $\bar{d}$ with other experiments at different values of $\sqrt{s_{NN}}$.

pion HBT (Fig. 5.3). It is found that the light nuclei freeze-out volume is proportional to the pion HBT results in different centrality collisions.

We have systematically studied the in heavy-ion collision systems at various energies [12, 90], shown in Fig. 7.2. The results indicate that the freeze-out volume increases with beam energy to a limit then it keeps as a flat value when the beam energy is larger than 20 GeV. The turn-over point is due to the collision system changes from a baryon rich system to a meson rich system [90].

The $d + \bar{d}$ v_2 at intermediate p_T region shows following the atomic mass number A scaling within error bars (Fig. 5.4). Our results indicate that the $^3He + \overline{^3He}$ v_2 deviates the baryon v_2 after A scaling on both v_2 and p_T, this might due to the higher order effect of the profile of the source. We can not draw further conclusions since the statistical error is large.

At low p_T ($0.2 < p_T < 0.5$ GeV/c), the $\bar{d}$ v_2 is found to be negative (Fig. 5.4) in mid-central collisions. This is the first negative observed at RHIC. The previous measurement shows the $\bar{p}$ v_2 is consistent with our results. However, the $\bar{p}$ v_2 has large errors and it also consistent with zero. We also compare our results to the blast-wave model. The model, which includes the large redial flow scenario, shows a negative flow, either. But the blast-wave model can not reproduce our data. In this model, there is only the mass input for light nuclei. There is no final-state coalescence processes for the formation of light nuclei. That is, the calculation only treats the nuclei, such as $\bar{d}$, as heavy particles that create early in the system evolution. Further study on the model and a better statistical measurements will lead us to a better understanding of the freeze-out dynamics.

In Chapter 6, we systematically studied the anti-baryon density from different collision systems. It is found that the gluon interactions are responsible for the anti-baryon creation. The results from $e^+ + e^-$ experiments also conclude that the $p(\bar{p})$ production is dominated by the gluon jets fragmentation while the light quark jets fragmentation contributes more to the $\pi^\pm$ production (See Chapter 1 for details).

In Chapter 1, we discussed the pQCD calculation for the energetic parton energy loss when they propagate the hot and dense medium. It indicates that the gluon energy loss is larger than that of quark while the light quarks (u, d, s) lose more energy than heavy quarks (c, b). Therefore, at high p_T region ($p_T > 5\ GeV/c$), one would expect the baryons be suppressed more than mesons. However, our measurement shows the suppression of baryons and mesons at high p_T are observed to be the same (See Fig. 4.2). Besides, as shown in Fig. 7.3, the R_{AA} of non-photonic electrons, which come from the heavy flavor hadrons (D, B, Λ_c) semileptonic decays, also have the similar values as hadrons at high p_T in central Au+Au collisions [68].

These results indicate that the partonic source of $\pi^\pm$, $p(\bar{p})$ and heavy flavor hadrons have similar energy loss when they transversing the nuclear medium. It is a new challenge to the understanding of energy loss and modified parton fragmentation in strongly interacting matter.

Recently, Wei Liu *et al.* attempted to explain our data by studying the compton-like gluon/quark jets conversion in the QGP [89]. Their calculations are shown in Fig. 7.4 and Fig. 7.5.

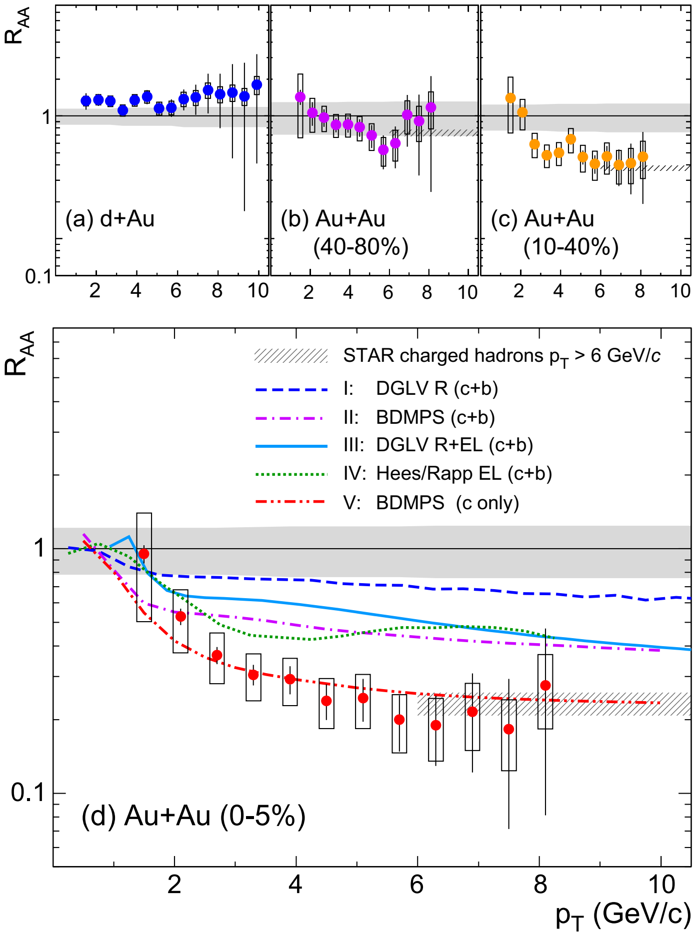

Figure 7.3: The non-photonic electrons R_{AA} as a function of centrality and p_T for d+Au and Au+Au collisions at $\sqrt{s_{NN}} = 200GeV$.

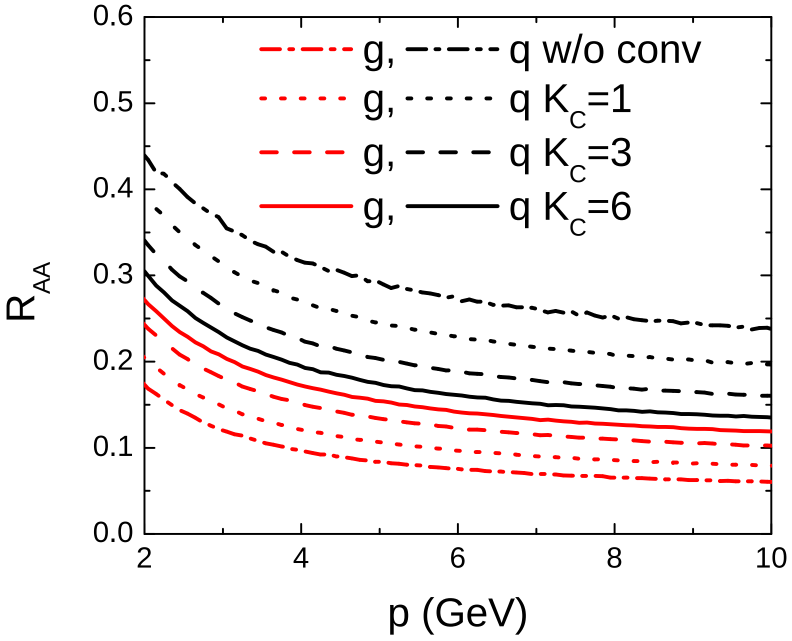

Figure 7.4: Nuclear modification factors for quark (upper lines) and gluon (lower lines) jets as functions of momentum without (dash-dotted lines) and with different enhancement factors $K_C = 1$ (dotted lines), $K_C = 3$ (dashed lines), and $K_C = 6$ (solid lines) for conversion scattering.

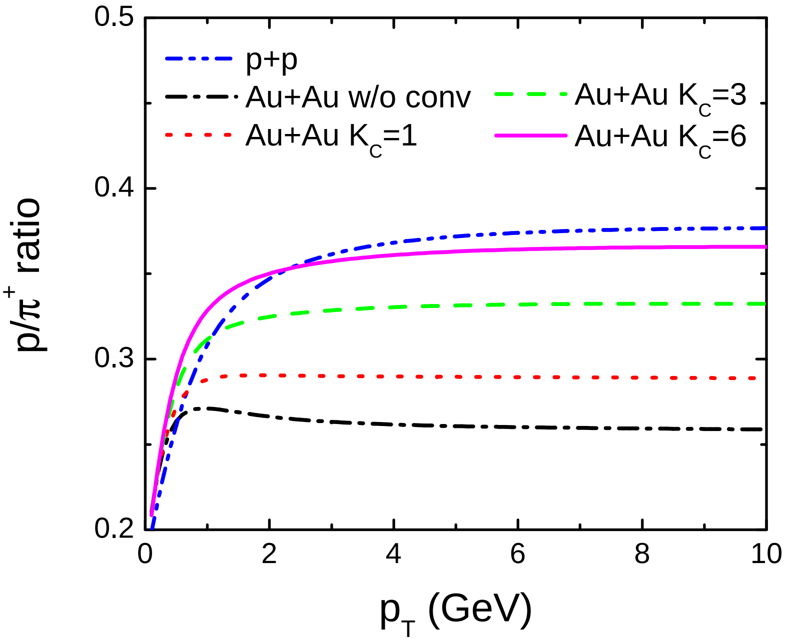

Figure 7.5: p/π^+ ratio from jet fragmentation in central Au+Au collisions at $\sqrt{s_{NN}} = 200\ GeV$ as a function of transverse momentum without (dash-dotted line) and with different enhancement factors $K_C = 1$ (dotted line), $K_C = 3$ (dashed line), and $K_C = 6$ (solid line) for conversion scattering. The dash-dot-dotted line corresponds to p+p collisions at same energy.

Fig. 7.4 shows the R_{AA} as a function of quarks and gluons. As we expected, the R_{AA} for gluons is much smaller than that for quarks as a result of larger energy loss for gluon jets than for quark jets. If we enhance the gluon/quark scattering cross section, the difference between the quark and gluon R_{AA} will be reduced.

In Fig. 7.5, it is shown that without gluon/quark conversion, the p/π^+ ratio in Au+Au collisions is significantly smaller than that in p+p collisions. If the enhance factor of 6 is applied to the conversion, the p/π^+ ratio in Au+Au collisions increases and gets close to the value of p+p collisions.

7.3 Future measurements

STAR has proposed a few important sub-detector (facility) upgrades such as a full barrel Time-Of-Flight, a Heavy Flavor Tracker, a Muon Telescope Detector, DAQ1000 system, and so on. One can imagine how many interesting topics and opportunities are waiting ahead. Here I would like to brief what we can achieve in the near future related to the results reported in this thesis.

With the precise secondary vertex reconstruction, which can be done by the HFT, we can easily separate the primordial p and $\bar{p}$ from weak decays. Therefore, this helps us a lot on the coalescence parameters calculation. By reducing the errors on B_2 and B_3 measurements, we will be able to study on the source profile, which can lead us to a better understanding of the system evolution and freeze-out conditions.

With the full barrel TOF and the future RHIC high statistic runs, we will be able to have a much better measurements on the light nuclei (d, t and ${}^3He$) v_2. We will have a better chance to further test the atomic mass number scaling and study the higher order effect of the final-state coalescence.

From the previous measurements, we found that the yield ratio of anti-nuclei has the relation of $\bar{p} : \bar{d} : \overline{{}^3He} \approx 10^6 : 10^3 : 1$ [91]. In the future with higher statistics, we should try to search for $\overline{{}^4He}$. This particle has never been observed before. The observation of $\overline{{}^4He}$ is important to the anti-matter theory and it will be a strong evidence for the coalescence. We should also try to search for the other high A anti-nuclei such as $\overline{{}^3_\Lambda H}$ ($\overline{{}^3_\Lambda H} \leftarrow \bar{p}+\bar{n}+\bar{\Lambda}$). $\overline{{}^3_\Lambda H}$ is the lightest antihypernuclei. It is unstable and can be searched by the identification of its decay products, which are $\overline{^3He}$ and π^+. The high PID capability and large acceptance of STAR open the door to the observation of those rare signals in the near future.

Appendix A

List of Publications

1. STAR Collaboration "Identified baryon and meson distributions at large transverse momenta from Au+Au collisions at $\sqrt{s_{NN}} = 200$ GeV" Phys. Rev. Lett. 97 (2006) 152301 e-Print Archives (nucl-ex/0606003) Principle author: Haidong Liu, Olga Barannikova, Lijuan Ruan and Zhangbu Xu

2. Haidong Liu, etc. "Extract the charm cross-section from its semileptonic decay at RHIC" Physics Letters B Vol.639 (2006) page 441-446 (e-print Arxiv: nucl-ex/0601030)

3. Haidong Liu "Yields and elliptic flow of d(dbar) and He3(He3bar) in Au+Au collisions at $\sqrt{s_{NN}} = 200$ GeV", contributed to 19th International Conference on Ultra Relativistic Nucleus-Nucleus Collisions (Quark Matter 2006), submitted to Journal of Physics G, e-print Arxiv: nucl-ex/0701057

4. Haidong Liu "Light nuclei production in Au+Au 200 GeV collisions at RHIC", contributed to XI International Workshop on Correlation and Fluctuation in Multiparticle Production (IWCF2006), submitted to International Journal of Modern Physics E

5. Haidong Liu and Zhangbu Xu "Universal anti-baryon density in e+e-,gp, pp, pA and AA collisions", submitted to Physics Letters B, e-print Arxiv: nucl-ex/0610035

6. YanE.Zhao, Xiaolian Wang, Haidong Liu, "Effect of Temperature on the Multi-gap Resistive Plate Chamber Operation", Nucle.Instr.and Meth A547 (2005) 334-341

7. YanE Zhao, Xiaolian Wang, Haidong Liu, “Dependence on Temperature and Voltage of MRPC noise and Dark Current”, HEP & NP, Vol28, N11, Nov., 2004

8. STAR Collaboration “Energy dependence of charged pion, proton and anti-proton transverse momentum spectra for Au+Au collisions at $\sqrt{s_{NN}} = 62.4$ and 200 GeV”, Submitted to Physics Letters B, e-Print Archives (nucl-ex/0703040)

9. STAR Collaboration “Mass, quark-number, and $\sqrt{s_{NN}}$ dependence of the second and fourth flow harmonics in ultra-relativistic nucleus-nucleus collisions”, Submitted to Phys. Rev. C, e-Print Archives (nucl-ex/0701010)

10. STAR Collaboration “The energy dependence of p_{t} angular correlations inferred from mean-p_{t} fluctuation scale dependence in heavy ion collisions at the SPS and RHIC”, J. Phys. G 34 (2007) 451, e-Print Archives (nucl-ex/0605021)

11. STAR Collaboration “Longitudinal Double-Spin Asymmetry and Cross Section for Inclusive Jet Production in Polarized Proton Collisions at $\sqrt{s_{NN}} = 200$ GeV”, Phys. Rev. Lett. 97 (2006) 252001, e-Print Archives (hep-ex/0608030)

12. STAR Collaboration “Neutral Kaon Interferometry in Au+Au collisions at $\sqrt{s_{NN}} = 200$ GeV”, Phys. Rev. C 74 (2006) 054902, e-Print Archives (nucl-ex/0608012)

13. STAR Collaboration “Delta-phi Delta-eta Correlations in Central Au+Au Collisions at $\sqrt{s_{NN}} = 200$ GeV”, Phys. Rev. C 75 (2007) 034901, e-Print Archives (nucl-ex/0607003)

14. STAR Collaboration “The multiplicity dependence of inclusive p_T spectra from p-p collisions at $\sqrt{s_{NN}} = 200$ GeV”, Phys. Rev. D 74 (2006) 032006, e-Print Archives (nucl-ex/0606028)

15. STAR Collaboration “Scaling properties of hyperon production in Au+Au collisions at $\sqrt{s_{NN}} = 200$ GeV”, Phys. Rev. Lett. 98 (2007) 062301, e-Print Archives (nucl-ex/0606014)

16. STAR Collaboration “Strange baryon resonance production in $\sqrt{s_{NN}} = 200$ GeV p+p and Au+Au collisions”, Phys. Rev. Lett. 97 (2006) 132301, e-Print Archives (nucl-ex/0604019)

17. STAR Collaboration “Direct observation of dijets in central Au+Au collisions

at $\sqrt{s_{NN}} = 200$ GeV", Phys. Rev. Lett. 97 (2006) 162301, e-Print Archives (nucl-ex/0604018)

18. STAR Collaboration "Forward Neutral Pion Production in p+p and d+Au Collisions at $\sqrt{s_{NN}}$=200 GeV", Phys. Rev. Lett. 97 (2006) 152302, e-Print Archives (nucl-ex/0602011)

19. STAR Collaboration "Identified hadron spectra at large transverse momentum in p+p and d+Au collisions at $\sqrt{s_{NN}} = 200$ GeV", Phys. Lett. B 637 (2006) 161, e-Print Archives (nucl-ex/0601033)

20. STAR Collaboration "Multiplicity and Pseudorapidity Distributions of Charged Particles and Photons at Forward Pseudorapidity in Au + Au Collisions at $\sqrt{s_{NN}} = 62.4$ GeV", Phys. Rev. C 73 (2006) 034906, e-Print Archives (nucl-ex/0511026)

21. STAR Collaboration "Proton - lambda correlations in central Au+Au collisions at $\sqrt{s_{NN}} = 200$ GeV", Phys. Rev. C 74 (2006) 064906, e-Print Archives (nucl-ex/0511003)

22. STAR Collaboration "Directed flow in Au+Au collisions at $\sqrt{s_{NN}} = 62$ GeV", Phys. Rev. C 73 (2006) 034903, e-Print Archives (nucl-ex/0510053)

23. STAR Collaboration "Transverse-momentum p_T correlations on (eta,phi) from mean p_T fluctuations in Au-Au collisions at $\sqrt{s_{NN}}) = 200$ GeV", J. Phys. G 32 (2006) L37, e-Print Archives (nucl-ex/0509030)

24. STAR Collaboration "Incident Energy Dependence of pt Correlations at RHIC", Phys. Rev. C 72 (2005) 044902, e-Print Archives (nucl-ex/0504031)

25. STAR Collaboration "Multi-strange baryon elliptic flow in Au+Au collisions at $\sqrt{s_{NN}} = 200$ GeV", Phys. Rev. Lett. 95 (2005) 122301, e-Print Archives (nucl-ex/0504022)

26. STAR Collaboration "Multiplicity and Pseudorapidity Distributions of Photons in Au + Au Collisions at $\sqrt{s_{NN}} = 62.4$ GeV", Phys. Rev. Lett. 95 (2005) 062301, e-Print Archives (nucl-ex/0502008)

Bibliography

[1] M. Schmelling. "Status of the strong coupling constant", 1996. hep-ex/9701002

[2] (Particle Data Group), D.E. Groom, et al. *Eur. Phys. Journal.*, **C15**:1, 2000.

[3] K. G. Wilson. *Phys. Rev.*, **D10**:2445, 1974.

[4] F. Karsch. "Lattice Results on QCD Thermodynamics." *Nucl. Phys.*, **A698**:199–208, 2002.

[5] J. Adams *et al.*, Nucl. Phys. A **757**, 102 (2005).

[6] J.L. Nagle *et al.*, Phys. Rev. C **53**, 367 (1996).

[7] R. Scheibl, U. Heinz, Phys. Rev. C **59**, 1585 (1999).

[8] W.J. Llope *et al.*, Phys. Rev. C **52**, 2004 (1995).

[9] R. Bond *et al.*, Phys. Lett. B **71**, 43 (1977); A. Baltz *et al.*, Phys. Lett. B **325**, 7 (1994); R. Mattiello *et al.*, Phys. Rev. C **55**, 1443 (1997); P. Braun-Munzinger *et al.*, Phys. Lett. B **334**, 43 (1995); A.Z. Mekjian, Phys. Rev. C **17**, 1051 (1978); H. Sato and K. Yazaki, Phys. Lett. B **98**, 153 (1981); J.I. Kapusta, Phys. Rev. C **21**, 1301 (1980).

[10] T.A. Armstrong *et al.*, Phys. Rev. C **61**, 064908 (2000);

[11] C. Adler *et al.*, Phys. Rev. Lett. **87**, 262301 (2001).

[12] S.S. Adler *et al.*, Phys. Rev. Lett. **94**, 122302 (2005).

[13] STAR Collaboration, J. Adams *et al.*, Phys. Rev. Lett. **92**, 052302 (2004).

[14] STAR Collaboration, J. Adams *et al.*, Phys. Rev. C **72**, 014904 (2005).

[15] DELPHI Collaboration, P. Abreu *et al.*, Eur. Phys. J. C **17**, 207 (2000).

[16] P.J. Siemens and J.I. Kapusta, Phys. Rev. Lett. **43**, 1486 (1979); Phys. Rev. Lett. **43**, 1690(E) (1979).

[17] L.P. Csernai and J.I. Kapusta, Phys. Rep. **131**, 223 (1986).

[18] F.Q. Wang and N. Xu, Phys. Rev. C **61**, 021904 (2000); F.Q. Wang, Phys. Lett. B **489**, 273 (2000).

[19] D.H. Boal and B.K. Jennings, Rev. Mod. Phys. **62**, 553 (1990).

[20] C.K. Gelbke, W.B. Bauer and S. Pratt, Annu. Rev. Nucl. Part. Sci. **42**, 77 (1992).

[21] CERES Collaboration, D. Adamová *et al.*, Phys. Rev. Lett. **90**, 022301 (2003).

[22] STAR Collaboration, C. Adler *et al.*, Phys. Rev. Lett. **89**, 202301 (2002).

[23] S. Wicks *et al.*, Nucl. Phys. A **784**, 426 (2007).

[24] N. Armesto *et al.*, Phys. Rev. D **71**, 054027 (2005).

[25] M. Djordjevic and M. Gyulassy Nucl. Phys. A **733**, 265 (2004).

[26] B. Hahn *et al.*, Phys. Rev. **101** (1956) 1131.

[27] STAR Collaboration, J. Adams *et al.*, Phys. Rev. Lett. **91**, 172302 (2003).

[28] PHENIX Collaboration, S.S. Adler *et al.*, Phys. Rev. Lett. **96**, 202301 (2006).

[29] C.Y. Wong *Introduction to High-Energy Heavy-Ion Collisions.* World Scientific Publishing Co. Pte. Ltd., 1994.

[30] http://www.rhic.bnl.gov/.

[31] T. Roser, Nuclear Physics A 688, 23c-28c, 2002.

[32] P. Sorenson, Ph.D. thesis, UCLA, 2003.

[33] H. Zhang, Ph.D. thesis, Yale University, 2003.

[34] J. Harris *et al.*, Nucl. Instrum. Meth. A **499**, 624 (2003).

[35] 'Conceptual Design Report for the Solenoidal Tracker At RHIC', The STAR Collaboration, PUB-5347 (1992); J.W. Harris et al, Nucl. Phys. A 566, 277c (1994).

[36] R.L. Brown et al., Proc. 1997 IEEE Particle Accelerator Conf., 3230 (1998) *and* F. Bergsma et al., 'The STAR Detector Magenet Subsystem', Nucl. Instrum. Meth. A499, 629 (2003).

[37] D. Lynn et al., Nucl. Instrum. Meth. A447, 264 (2000) *and* R. Bellwied et al., 'The STAR Silicon Vertex Tracker', Nucl. Instrum. Meth. A499, 636 (2003).

[38] L. Arnold et al., 'The STAR Silicon Strip Detector', Nucl. Instrum. Meth. A499, 648 (2003).

[39] H. Wieman et al., IEEE Trans. Nucl. Sci. 44, 671 (1997).

[40] M. Anderson *et al.*, Nucl. Instr. Meth. A **499**, 659 (2003).

[41] A. Schuttauf et al., Nuc. Phys. A661, 677c (1999) *and* K.H. Ackerman et al., 'The Forward Time Projection Chamber in STAR', Nucl. Instrum. Meth. A499, 709 (2003).

[42] 'A Ring Imaging Cherenkov Detector for STAR', STARnote 349, STAR/ALICE RICH Collaboration (1998); ALICE Collaboration, Technical Design and Report, Detector for High Momentum PID, CERN/LHCC 98-19.

[43] W.J. Llope *et al.*, Nucl. Instr. Meth. A **522**, 252 (2004).

[44] B. Bonner *et al.*, Nucl. Instr. Meth. A **508**, 181 (2003); M. Shao *et al.*, Nucl. Instr. Meth. A **492**, 344 (2002).

[45] STAR Collaboration, J. Adams *et al.*, Phys. Lett. B **616**, 8 (2005).

[46] STAR Collaboration, "proposal for a large area time of flight system for STAR".

[47] L.J. Ruan, Ph.D. thesis, University of Science and Technology of China, 2004.

[48] STAR Collaboration, J. Adams *et al.*, Phys. Rev. Lett. **92**, 112301 (2004).

[49] H. Long, Ph.D. thesis, UCLA, 2002.

[50] CERN RD44 Project at http://wwwinfo.cern.ch/asd/geant/geant4public/G4UsersDocuments/Welcome/IntroductionToGeant4/html/introductionToGeant4.html.

[51] P. Nevski, http://www.star.bnl.gov/STARAFS/comp/simu/gstar/gstar.html.

[52] S. Eidelman *et al.*, Phys. Lett. B **592**, 1 (2004).

[53] C. Struck,, Ph.D. thesis, University of Frankfurt, 2003.

[54] A.M. Poskanzer and S.A. Voloshin. *Phys. Rev. C*, **58**:1671, 1998.

[55] I. Vitev, Phys. Lett. B **639**, 38 (2006), curves are calculations with initial gluon rapidity density 1150 in 0-10% Au+Au and between 100 and 150 in 40-80% Au+Au collisions.

[56] STAR Collaboration, J. Adams *et al.*,Phys. Lett. B **637**, 161 (2006).

[57] X.N. Wang, Phys. Rev. C **58**, 2321 (1998); Q. Wang et al., Phys. Rev. C **71**, 014903 (2005).

[58] P. Abreu *et al.*, Eur. Phy. J. C **5**, 585 (1998).

[59] R.C. Hwa *et al.*, Phys. Rev. C **70**, 024905 (2004).

[60] R.J. Fries *et al.*, Phys. Rev. C **68**, 044902 (2003).

[61] PHENIX Collaboration, K. Adcox *et al.*, Phys. Rev. Lett. **88**, 242301 (2002); PHENIX Collaboration, S.S. Adler *et al.*, Phys. Rev. Lett. **91**, 172301 (2003). STAR Collaboration, J. Adams *et al.*, nucl-ex/0601042.

[62] D. Molnar *et al.*, Phys. Rev. Lett. **91**, 092301 (2003).

[63] V. Greco *et al.*, Phys. Rev. Lett. **90**, 202302 (2003).

[64] B.A. Kniehl *et al.*, Nucl. Phys. B **597**, 337 (2001). Fragmentation functions from this parameterization are called KKP.

[65] P.B. Straub *et al.*, Phys. Rev. D **45**, 3030 (1992).

[66] S. Albino *et al.*, Nucl. Phys. B **725**, 181 (2005). Fragmentation functions from this parameterization are called AKK.

[67] PHENIX Collaboration, S.S. Adler *etal.*, Phys. Rev. Lett. **96**, 032301 (2006).

[68] STAR Collaboration J. Adams *et al.*, e-print Arxiv: nucl-ex/0607012.

[69] M. Djordjevic *et al.*, Phys. Lett. B **632**, 81 (2006).

[70] A. Dainese *et al.*, Eur. Phys. J. C **38**, 461 (2005); K. Eskola et al., Nucl. Phys. A **747**, 511 (2005).

[71] STAR Collaboration, J. Adams *et al.*, Phys. Rev. **C71** (2005) 044906.

[72] X. Dong *et al.*, Phys. Lett. **B597** (2004) 328.

[73] P.J. Siemens and J.I. Kapusta, Phys. Rev. Lett. **43**, 1486 (1979); **43,** 1690(E) (1979); L.P. Csernai and J.I. Kapusta, Phys. Rep. **131,** 223 (1986).

[74] F.Binon *et al.*, Phys. Lett. B **30**, 510 (1969).

[75] J.A. Appel *et al.*, Phys. Rev. Lett. **32**, 428 (1974).

[76] B. Alper *et al.*, Phys. Lett. B **46**, 265 (1973).

[77] T. Alexopoulos *et al.*, Phys. Rev. D **62**, 072004 (2000).

[78] M. Aoki *et al.*, Phys. Rev. Lett. **69**, 2345 (1992).

[79] T.A. Armstrong *et al.*, Phys. Rev. Lett. **85**, 2685 (2000).

[80] G. Ambrosini *et al.*, New J. Phys. **1**, 22.1 (1999); Heavy Ion Phys. **14** 297 (2001), e-print arxiv: nucl-ex/0011016.

[81] I.G. Bearden *et al.*, Phys. Rev. Lett. **85**, 2681 (2000).

[82] C. Adler *et al.*, Phys. Rev. Lett. **87**, 262301 (2001).

[83] S.S. Adler *et al.*, Phys. Rev. Lett. **94**, 122302 (2005).

[84] C. Adler *et al.*, Phys. Rev. Lett. **86**, 4778 (2001); L. Ahle *et al.*, Phys. Rev. Lett. **81**, 2650 (1998); F. Sickler *et al.*, Nucl. Phys. A **661**, 45c (1999); G. E. Copper, Ph.D Thesis, University of California at Berkeley, 2000; A.M. Rossi *et al.*, Nucl. Phys. B **84**, 269 (1975); M. Aguilar-Benitez *et al.*, Z. Phys. C **50**, 405 (1991).

[85] H. Albrecht *et al.*, Phys. Lett. B **236**, 102 (1990).

[86] A. Aktas *et al.*, Eur. Phys. J. C **36**, 413 (2004).

[87] S.Schael *et al.*, Phys. Lett. B **639**, 192 (2006), e-print Arxiv: hep-ex/0604023.

[88] STAR Collaboration J. Adams *et al.*, e-print Arxiv: nucl-ex/0601042.

[89] W. Liu *et al.*, e-print Arxiv: nucl-th/0607047.

[90] S. Wang *et al.*, Phys. Rev. Lett. **74**, 2646 (1995); S. Albergo *et al.*, Phys. Rev. C **65**, 034907 (2002); T.A. Armstrong *et al.*, Phys. Rev. Lett. **85**, 2685 (2000); T. Anticic *et al.*, Phys. Rev. C **69**, 024902 (2004); I.G. Bearden *et al.*, Phys. Rev. Lett. **85**, 2681 (2000).

[91] H. Liu and Z. Xu, e-print Arxiv: nucl-ex/0610035; Z. Xu, e-print Arxiv: nucl-ex/0207019.